Cancer cells with defective oxidative phosphorylation require endoplasmic reticulum–to–mitochondria Ca 2+ transfer for survival

Article *in* Science Signaling · July 2020

DOI: 10.1126/scisignal.aay1212

20 authors, including:

Cesar Cardenas
University of Chile
71 PUBLICATIONS **2,672** CITATIONS
SEE PROFILE

Alenka Lovy
Tufts University
23 PUBLICATIONS **1,064** CITATIONS
SEE PROFILE

Eduardo Silva Pavez
Universidad Mayor
28 PUBLICATIONS **163** CITATIONS
SEE PROFILE

Félix A Urra
University of Chile
36 PUBLICATIONS **327** CITATIONS
SEE PROFILE

METABOLISM

Cancer cells with defective oxidative phosphorylation require endoplasmic reticulum–to–mitochondria Ca^{2+} transfer for survival

Cesar Cardenas[1,2,3,4]*†‡, Alenka Lovy[1,2,5]*, Eduardo Silva-Pavez[1,2], Felix Urra[2,6], Craig Mizzoni[7], Ulises Ahumada-Castro[1,2], Galdo Bustos[1,2], Fabian Jaňa[2,8], Pablo Cruz[1,2], Paula Farias[1,2], Elizabeth Mendoza[1,2], Hernan Huerta[1,2], Paola Murgas[1], Martin Hunter[7], Melany Rios[1,2], Oscar Cerda[9,10,11], Irene Georgakoudi[7], Armen Zakarian[4], Jordi Molgó[12], J. Kevin Foskett[13]†‡

Spontaneous Ca^{2+} signaling from the $InsP_3R$ intracellular Ca^{2+} release channel to mitochondria is essential for optimal oxidative phosphorylation (OXPHOS) and ATP production. In cells with defective OXPHOS, reductive carboxylation replaces oxidative metabolism to maintain amounts of reducing equivalents and metabolic precursors. To investigate the role of mitochondrial Ca^{2+} uptake in regulating bioenergetics in these cells, we used OXPHOS-competent and OXPHOS-defective cells. Inhibition of $InsP_3R$ activity or mitochondrial Ca^{2+} uptake increased α-ketoglutarate (αKG) abundance and the NAD^+/NADH ratio, indicating that constitutive endoplasmic reticulum (ER)–to–mitochondria Ca^{2+} transfer promoted optimal αKG dehydrogenase (αKGDH) activity. Reducing mitochondrial Ca^{2+} inhibited αKGDH activity and increased NAD^+, which induced SIRT1-dependent autophagy in both OXPHOS-competent and OXPHOS-defective cells. Whereas autophagic flux in OXPHOS-competent cells promoted cell survival, it was impaired in OXPHOS-defective cells because of inhibition of autophagosome-lysosome fusion. Inhibition of αKGDH and impaired autophagic flux in OXPHOS-defective cells resulted in pronounced cell death in response to interruption of constitutive flux of Ca^{2+} from ER to mitochondria. These results demonstrate that mitochondria play a fundamental role in maintaining bioenergetic homeostasis of both OXPHOS-competent and OXPHOS-defective cells, with Ca^{2+} regulation of αKGDH activity playing a pivotal role. Inhibition of ER-to-mitochondria Ca^{2+} transfer may represent a general therapeutic strategy against cancer cells regardless of their OXPHOS status.

INTRODUCTION

Many cancers switch from oxidative phosphorylation (OXPHOS) to glycolysis as the main source of adenosine triphosphate (ATP) generation in the presence of ample oxygen, a phenomenon known as the Warburg effect (*1*). Although enhanced aerobic glycolysis has been misinterpreted as a sign of mitochondrial dysfunction in cancer cells, fully functional mitochondria are needed in many cancer cell types (*2*–*5*). Oncogene activation increases mitochondrial metabolism, and anchorage-independent growth and metastatic potential are correlated with mitochondrial function (*2*, *6*). In addition to its role in ATP production by OXPHOS, mitochondria fuel biosynthetic pathways through the tricarboxylic acid (TCA) cycle to produce lipids, proteins, and nucleic acids required in highly proliferating cells (*3*, *4*, *7*–*11*). Many studies have targeted OXPHOS as a therapeutic strategy in cancer (*12*–*15*).

In rapidly proliferating cells and many cancer cells as well as in cells with defective OXPHOS, including those caused by mutations in either fumarate hydratase or components of succinate dehydrogenase, reductive carboxylation of glutamine-derived α-ketoglutarate (αKG) by nicotinamide adenine dinucleotide (NAD^+) phosphate ($NADP^+$)/reduced form of $NADP^+$ (NADPH)–dependent isocitrate dehydrogenase (IDH1 and IDH2) generates citrate. Citrate, in turn, provides acetyl–coenzyme A (CoA) for lipid synthesis and for replenishing TCA cycle intermediates (*16*, *17*), including aspartate for nucleotide synthesis, by its cleavage to form oxaloacetate and its transamination (*18*, *19*). In OXPHOS-defective 143BΔcytb cybrid cells and other cells with defective OXPHOS, the reducing equivalents needed for the reductive carboxylation reaction are generated by oxidation of αKG by αKG dehydrogenase (αKGDH). Thus, oxidative metabolism persists and coexists in 143BΔcytb cells and other cell lines that use reductive carboxylation (*17*, *20*). αKGDH activity is under complex regulation by substrate levels and cofactors (*21*), including mitochondrial matrix Ca^{2+} concentration. Ca^{2+} increases the affinity of αKGDH for its substrate, enhancing its activity over 100-fold (*22*).

Low-level constitutive Ca^{2+} release from the endoplasmic reticulum (ER) through inositol 1,4,5-trisphosphate receptors ($InsP_3Rs$) is

[1]Center for Integrative Biology, Faculty of Sciences, Universidad Mayor, Santiago 8580745, Chile. [2]Geroscience Center for Brain Health and Metabolism, Santiago 8580745, Chile. [3]Buck Institute for Research on Aging, Novato, CA 94945, USA. [4]Department of Chemistry and Biochemistry, University of California, Santa Barbara, Santa Barbara, CA 93106, USA. [5]Department of Neuroscience, Center for Neuroscience Research, Tufts University School of Medicine, Boston, MA 02111, USA. [6]Program of Molecular and Clinical Pharmacology, Institute of Biomedical Science, Universidad de Chile, Santiago 8380453, Chile. [7]Department of Biomedical Engineering, Tufts University, Medford, MA 02155, USA. [8]Universidad de Aysén, Coyhaique, 5952073, 8380453, Chile. [9]Program of Cellular and Molecular Biology, Institute of Biomedical Sciences (ICBM), Faculty of Medicine, Universidad de Chile, Santiago, Chile. [10]Millennium Nucleus of Ion Channels-Associated Diseases (MiNICAD), Santiago, Chile. [11]The Wound Repair, Treatment and Health (WoRTH), Santiago, Chile. [12]Université Paris-Saclay, CEA, Institut des Sciences du Vivant Frédéric Joliot, ERL CNRS n° 9004, Département Médicaments et Technologies pour la Santé, Service d'Ingénierie Moléculaire pour la Santé (SIMoS), bâtiment 152, Point courrier 24, F-91191 Gif sur Yvette, France. [13]Departments of Physiology and Cell and Developmental Biology, Perelman School of Medicine, University of Pennsylvania, Philadelphia, PA 19104, USA.

*These authors contributed equally to this work.

†These authors contributed equally as co-senior authors.

‡Corresponding author. Email: julio.cardenas@umayor.cl (C.C.); foskett@pennmedicine.upenn.edu (J.K.F.)

essential to maintain OXPHOS (*23*). Inhibition of $InsP_3R$ activity reduces the O_2 consumption rate (OCR), lowers cell ATP levels, and activates adenosine monophosphate (AMP)–activated protein kinase (AMPK)–dependent, mechanistic target of rapamycin (mTOR)–independent prosurvival autophagy. A similar and nonadditive response is elicited by inhibition of mitochondrial Ca^{2+} uptake by the Ca^{2+} uniporter (*24*–*26*), the major pathway for Ca^{2+} uptake into the mitochondrial matrix (*27*). Thus, constitutive low-level ER-to-mitochondrial Ca^{2+} transfer is required to preserve normal bioenergetics by regulation of OXPHOS. Here, we demonstrated that constitutive $InsP_3R$-mediated Ca^{2+} signaling to mitochondria was required to maintain mitochondrial bioenergetics even in the absence of OXPHOS. In cells with defective OXPHOS, constitutive low-level mitochondrial Ca^{2+} uptake sustained the oxidative activity of the αKGDH complex to maintain reduced form of NAD^+ (NADH) levels to support reductive carboxylation. In its absence, NAD^+/NADH levels increased and autophagy was activated in a SIRT1-dependent manner. Autophagy promoted survival in cells with competent OXPHOS, but it was insufficient in OXPHOS-defective cells because of defective autophagosome-lysosome fusion. These results indicate that constitutive ER-to-mitochondria Ca^{2+} transfer regulates cellular bioenergetics regardless of the OXPHOS status and suggest that targeting mitochondrial Ca^{2+} uptake may provide a strategy to kill cancer cells by impinging on multiple pathways regulating mitochondrial metabolism.

RESULTS

Viability of OXPHOS-defective cells requires constitutive $InsP_3R$-mediated Ca^{2+} release

To determine the role of constitutive low-level $InsP_3R$-mediated Ca^{2+} release on bioenergetics of cells with defective OXPHOS, we used cybrids derived from 143B osteosarcoma cells in which mitochondrial DNA had been depleted (p^0) and then reconstituted with either wild-type mitochondrial DNA (143Bwt) or with mitochondrial DNA containing a 4–base pair mutation in the cytochrome *b* gene (143BΔcytb). In the 143BΔcytb cells, the flow of electrons stops at complex III (*6*), rendering mitochondria unable to reduce O_2 and produce ATP. Compared with 143Bwt cells, 143BΔcytb cells had lower basal OCR (Fig. 1A) but higher basal extracellular acidification rate (ECAR), a measure of glycolysis (Fig. 1B), as expected. Although 143Bwt cells are cancer derived and activation of the Warburg effect was expected, they nevertheless use mitochondria for OXPHOS, as observed in other cancer cells (*8*, *9*, *12*, *24*, *28*–*31*). ATP content in basal conditions was similar in 143Bwt and 143BΔcytb cells (Fig. 1C). Inhibition of respiratory complexes III or V with antimycin A and oligomycin, respectively, did not affect ATP content in 143BΔcytb cells, whereas 2-deoxyglucose (2DG) did, confirming that glycolysis provided the main source of ATP in these cells. In contrast, these inhibitors reduced ATP levels in 143Bwt cells (Fig. 1C).

Like normal cells (*23*), cancer cells require constitutive $InsP_3R$-mediated Ca^{2+} transfer to mitochondria for optimal mitochondrial function and viability (*24*). Both 143Bwt and 143BΔcytb cells exhibited similar constitutive Ca^{2+} release activity that was $InsP_3R$ dependent, as shown by the suppression of this activity by the specific $InsP_3R$ inhibitor xestospongin B (XeB) (Fig. 1, D and E) (*32*). The cytoplasmic free Ca^{2+} concentration ($[Ca^{2+}]_i$) and mitochondrial matrix free Ca^{2+} concentration ($[Ca^{2+}]_m$) responses to histamine stimulation were similar in 143BΔcytb and 143Bwt cells (Fig. 1, F and G) despite a lower mitochondrial membrane potential ($\Delta\Psi_m$) in the 143BΔcytb cells (fig. S1A), as has been previously observed (*33*). Knockdown of mitochondrial calcium uniporter (MCU), the pore-forming subunit of the mitochondrial Ca^{2+} uniporter, prevented mitochondrial Ca^{2+} uptake (fig. S1, B and C). Labeling with nonyl acridine orange (NAO) revealed no differences in the numbers of mitochondria betweeen143Bwt and 143BΔcytb cells (fig. S1D). XeB decreased the OCR and ATP levels in 143Bwt cells, as observed in other cancer and normal cell types (*23*, *24*) but not in 143BΔcytb cells (Fig. 1, A and C). XeB did not change the rate of ECAR in either cell line (Fig. 1B). In tumorigenic breast and prostate cells with functional mitochondria, prolonged inhibition of $InsP_3R$ by XeB generates a bioenergetic crisis that results in >70% cell death (*24*). Because 143BΔcytb cells rely mainly on glycolysis, it was expected that they would be resistant to XeB-induced death. However, XeB caused cytotoxicity, with the 143BΔcytb cells significantly more sensitive than 143Bwt cells (Fig. 1H).

To confirm that the observed effects of XeB were specifically due to inhibition of $InsP_3R$ activity, types 1 and 3 $InsP_3Rs$ were simultaneously knocked down by mixing pools of four small interfering RNAs (siRNAs) against each of the types 1 and 3 $InsP_3Rs$ (IP3R1 + 3), generating >80 and 90% knockdown in 143Bwt and 143BΔcytb cells, respectively (Fig. 2A). $InsP_3R$ knockdown reduced basal OCR in 143Bwt cells but not in 143BΔcytb cells (Fig. 2B). In contrast, cell death was enhanced in both lines, with 143BΔcytb cells being more sensitive (Fig. 2C), similar to their greater sensitivity to XeB. Similar results were observed when types 1 and 3 $InsP_3Rs$ were simultaneously knocked down with a single siRNA designed to recognize both isoforms (IP3R1 and IP3R3) (fig. S1, E to G). These results suggest that 143BΔcytb cells, despite defective OXPHOS, require low-level constitutive $InsP_3R$ Ca^{2+} release for survival. The type 3 $InsP_3R$ has been associated with apoptosis resistance in cancer (*34*, *35*). However, knockdown of only this isoform (>80% in both cell lines; fig. S1, H and I) did not affect basal OCR (fig. S1J) or cell viability (fig. S1K) in either cell line, in agreement with the previous observation that the expression of either type 1 or type 3 $InsP_3R$ is sufficient to maintain cellular bioenergetics (*23*). To determine if $InsP_3R$ activity provided Ca^{2+} for mitochondrial uptake, we knocked down (~80%) the expression of MCU with two different siRNAs (Fig. 2, D and E). Knockdown of MCU with each siRNA reduced OCR in 143Bwt cells but not in 143BΔcytb cells (Fig. 2, F and G), phenocopying the effects of XeB and $InsP_3R$ knockdown. In both cell lines, significant cell death was observed, which was again more profound in the 143BΔcytb cells (Fig. 2, H and I), exceeding that caused by $InsP_3R$ inhibition. These results suggest that although 143BΔcytb cells do not use mitochondria to generate ATP, $InsP_3R$-mediated Ca^{2+} transfer to mitochondria is nevertheless essential to maintain their viability.

XeB reduced $\Delta\Psi_m$ in 143Bwt cells but not in 143BΔcytb cells (fig. S1A), which suggested that XeB-induced cytotoxicity of 143BΔcytb cells was not caused by loss of $\Delta\Psi_m$. 143BΔcytb cells have been reported to have higher resting levels of reactive oxygen species (ROS) compared with 143Bwt cells (*36*). Although increased ROS generation can cause cell death (*37*), we detected no differences in ROS levels between143Bwt and 143BΔcytb cells in resting and XeB-treated conditions (fig. S1L), in agreement with other reports (*6*, *38*). Furthermore, XeB-induced cell death was not affected by the ROS scavenger *N*-acetylcysteine (NAC) (fig. S1M).

Although 143BΔcytb cells have defective OXPHOS, they require the TCA cycle for glutamine metabolism through reductive carboxylation (*6*).

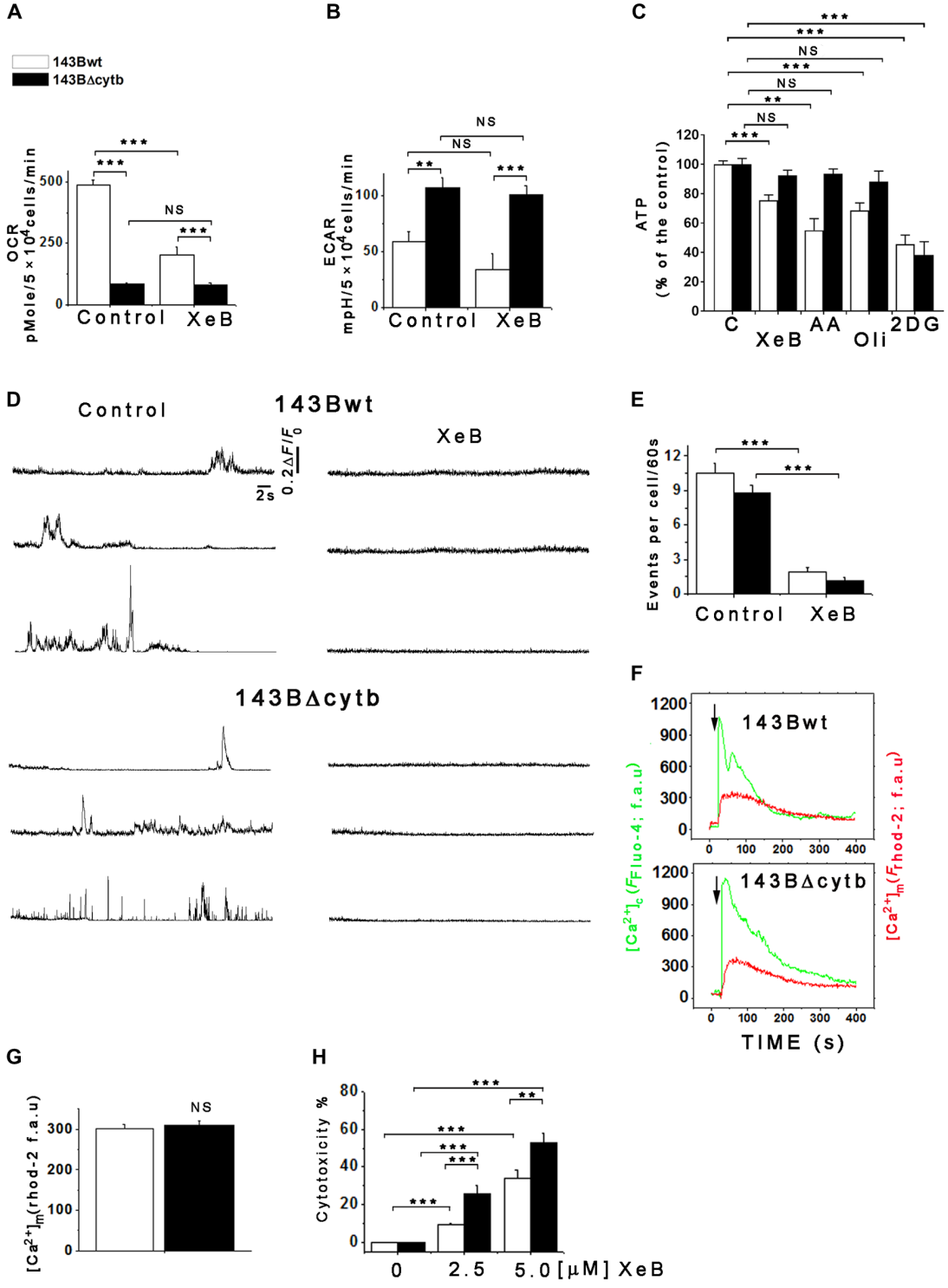

Fig. 1. OXPHOS-defective 143BΔcytb cells rely on constitutive $InsP_3R$-mediated Ca^{2+} signals. (**A**) Basal oxygen consumption rate (OCR) of cells incubated with 5 μM XeB for 4 hours. (**B**) Extracellular acidification rate (ECAR) of cells incubated with 5 μM XeB for 4 hours. Data in (A) and (B) represent means ± SEM of three independent experiments with 10 replicates each. $^{**}P < 0.01$ and $^{***}P < 0.001$ compared to respective control. NS, not significant. (**C**) Cells were incubated with 5 μM XeB, 1 μM antimycin A (AA) or 1 μM oligomycin (Oli), 2-deoxyglucose (2DG; 20 mM), or vehicle control (C) for 4 hours, and intracellular ATP levels were determined. Means ± SEM of three independent experiments performed in triplicate. $^{***}P < 0.001$ compared to control. (**D**) Representative recordings of Ca^{2+} release events in unstimulated cells treated or not with 5 μM XeB for 30 min. (**E**) Quantification of Ca^{2+} release events. Means ± SEM of three independent experiments. From each experiment, 30 cells were analyzed. (**F**) Representative traces of $[Ca^{2+}]_c$ (green) and $[Ca^{2+}]_m$ (red) responses in 143Bwt and 143BΔcytb cells challenged with histamine (100 μM). (**G**) Quantification of peak rhod-2 fluorescence. Means ± SEM of three independent experiments. In each experiment, 100 cells were analyzed. (**H**) Cells were treated with 2.5 or 5 μM XeB for 12 hours, and death was determined by LDH release. Means ± SEM of three independent experiments each with six replicates. $^{**}P < 0.01$ and $^{***}P < 0.001$.

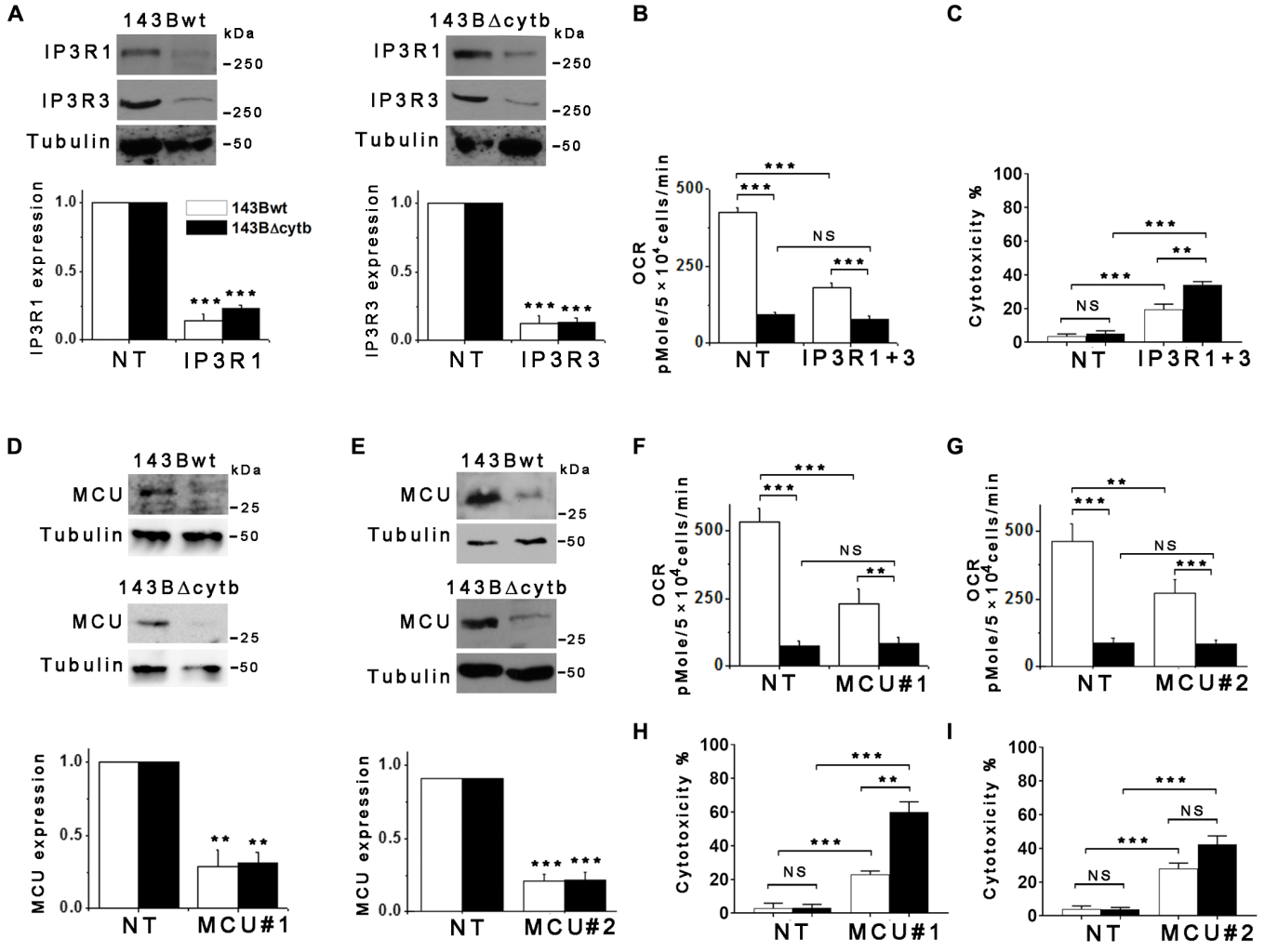

Fig. 2. Simultaneous knockdown of types 1 and 3 $InsP_3R$ or mitochondrial Ca^{2+} uptake induces cell death in OXPHOS-defective 143BΔcytb cells. (**A**) Representative Western blots of types 1 and 3 $InsP_3R$ in cells transiently transfected with a pool of four siRNAs against type 1 $InsP_3R$ and a pool of four siRNAs against type 3 $InsP_3R$ (IP3R1 + 3) or a nontargeting (NT) siRNA for 24 hours. (**B**) Basal OCR of cells transiently transfected with siRNAs against types 1 and 3 $InsP_3R$ (IP3R1 + 3) or nontargeting siRNA for 24 hours. Means ± SEM of three independent experiments with 10 replicates each. ***$P < 0.001$ compared to control. (**C**) Cell death as assessed by LDH release in cells transiently transfected with siRNAs targeting types 1 and 3 $InsP_3R$ (IP3R1 + 3) or nontargeting siRNA for 24 hours. Means ± SEM of three independent experiment each with six replicates. ***$P < 0.001$. (**D**) Representative Western blots of MCU in cells transiently transfected with MCU siRNA#1 or nontargeting siRNA for 72 hours. (**E**) Representative Western blots of MCU in cells transiently transfected with MCU siRNA#2 or nontargeting siRNA for 72 hours. (**F**) Basal OCR of cells transiently transfected with MCU siRNA#1 or nontargeting siRNA for 72 hours. (**G**) Basal OCR of cells transiently transfected with MCU siRNA#2 or nontargeting siRNA for 72 hours. (**H**) Cell death as assessed by LDH release in cells transiently transfected with MCU siRNA#1 or a nontargeting siRNA for 72 hours. (**I**) Cell death as assessed by LDH release in cells transiently transfected with MCU siRNA#2 or a nontargeting siRNA for 72 hours. In (A), bar graphs represent IP3R1 and IP3R3 expression normalized to tubulin. In (D) and (E), bar graphs represent MCU expression normalized to tubulin. Data in (A), (D), and (E) are means ± SEM of three independent biological replicates. **$P < 0.01$ and ***$P < 0.001$ compared with respective controls (NT). Data in (B), (F), and (G) represent means ± SEM of three independent experiments with 10 replicates each. **$P < 0.01$ and ***$P < 0.001$ compared to respective controls (NT). Cytotoxicity data in (C), (H), and (I) are means ± SEM of three independent experiments, each with six replicates. **$P < 0.01$ and ***$P < 0.001$ compared with respective controls (NT).

We therefore asked whether the requirement for constitutive Ca^{2+} transfer from the ER to mitochondria was specific to the 143BΔcytb cells or if it could be recapitulated in other cells that exhibit OXPHOS deficiency. The RCC4 human renal carcinoma cell line has a von Hippel–Lindau (*vhl*) mutation that results in constitutive activation of hypoxia-inducible factors, repression of mitochondrial function and OCR, and activation of reductive carboxylation (fig. S2A) (*39*). RCC4 cells were significantly more sensitive to XeB-induced toxicity than RCC4 cells expressing normal *vhl*, with cell death reaching ~70% after 12 hours (fig. S2, B and C). XeB-sensitive basal Ca^{2+} release activity was similar in RCC4 cells and RCC4 cells expressing *vhl* (fig. S2D). Thus, constitutive Ca^{2+} transfer from ER to mitochondria is required in both 143BΔcytb and RCC4 cells that exhibit OXPHOS deficiency.

Inhibition of constitutive $InsP_3R$-mediated Ca^{2+} release suppresses αKGDH activity

Like many cancer cells, 143BΔcytb cells rely on reductive carboxylation to generate metabolites for growth and proliferation (*16*–*19*). When oxidation of metabolites in the TCA cycle is unfavorable, such as

when OXPHOS activity is defective, glutamine provides glutamate through glutaminase activity, which is converted by glutamate dehydrogenases or aminotransferases to αKG (*2*). αKG is oxidized by αKGDH to succinyl-CoA to generate the reducing equivalents for IDH2-mediated reductive carboxylation of αKG to isocitrate (*20*) and other intermediates for production of TCA cycle metabolites (*40*). In addition, the reductive carboxylation of glutamine fuels compensatory aspartate synthesis from αKG through a pathway that requires the aspartate aminotransferase GOT1 (*18*, *19*). Removal of glutamine was cytotoxic for 143BΔcytb cells, which was rescued by the addition of dimethyl-α-ketoglutarate (Fig. 3A), which can be readily used by αKGDH to sustain levels of metabolic intermediates. Furthermore, preventing the conversion of glutamate to αKG by inhibiting transaminases or glutamate dehydrogenase 1 with aminooxyacetate (AOA) or epigallocatechin gallate (EGCG), respectively, was much more cytotoxic for 143BΔcytb cells than for 143Bwt cells (Fig. 3, B and C). Unexpectedly, inhibition of glutaminase with CB839 reduced the viability of both cell lines (Fig. 3D). Nevertheless, these results indicate a reliance of 143BΔcytb cells on αKGDH activity, likely for the generation of NADH to maintain reductive carboxylation. In agreement, inhibition of αKGDH activity with CPI-613 had a significantly higher cytotoxic effect on 143BΔcytb cells (Fig. 3E).

Because αKGDH is Ca^{2+} sensitive, we hypothesized that the cytotoxic effects of blocking ER-to-mitochondrial Ca^{2+} transfer in cells reliant on reductive carboxylation was caused by suppression of αKGDH activity. Exposure to XeB resulted in accumulation of αKG (Fig. 3F), consistent with a requirement of αKGDH activity on constitutive mitochondrial Ca^{2+} uptake, as observed for pyruvate dehydrogenase (PDH) (*23*). This result suggested that the inhibition of ER Ca^{2+} transfer to the mitochondria likely induced metabolic remodeling. A previous metabolomics study comparing the abundance of more than 90 metabolites between 143Bwt and 143BΔcytb revealed relatively minor differences between the two cell lines (*20*). We performed a metabolomics study to compare the abundance of metabolites from glycolysis, the pentose phosphate pathway, one-carbon/nucleotide metabolism, the TCA cycle, and other pathways in 143BΔcytb cells treated or not with XeB for 4 hours. Principal components analysis (fig. S3A) and hierarchical clustering (fig. S3B) revealed significant differences between the two groups. Analyses of metabolic intermediates generated by reductive carboxylation downstream of αKGDH revealed that succinate, malic acid, and citrate-isocitrate were significantly reduced after XeB treatment (Table 1), consistent with a decrease in αKGDH activity. These results suggest that inhibition of ER to mitochondria Ca^{2+} transfer alters the metabolic profile of 143BΔcytb cells, including a reduction in αKGDH activity.

To confirm the importance of Ca^{2+} in the regulation of αKGDH activity and its pivotal role in cell survival in cells with defective OXPHOS, we mutated aspartic acid at residue 154 to alanine (D154A) in the Ca^{2+}-binding site of the E1-αKGDH subunit. This mutation decreases the Ca^{2+} sensitivity of αKGDH activity by sixfold (*41*). We hypothesized that overexpression of the E1-αKGDH mutant would decrease αKGDH activity and consequently reduce cell viability, mimicking the effects observed after the inhibition of Ca^{2+} transfer to mitochondria. As a control, we overexpressed E179A E1-αKGDH (fig. S2E), which has a Ca^{2+} sensitivity similar to the wild-type enzyme. All expressed proteins localized to the mitochondria (fig. S2F). Viability did not differ between overexpressing cells grown in glucose-rich culture media (Fig. 3G). However, when cells were cultured for 24 hours with glutamine as the only carbon source, the cells expressing the D154A mutant had significantly decreased viability, whereas the E179A-expressing and wild-type E1-αKGDH–expressing cells were unaffected (Fig. 3G). This result confirms that mitochondrial Ca^{2+} is critical for promoting sufficient αKGDH activity to maintain cell viability, and it complements the results achieved by genetic and pharmacological inhibition of mitochondrial Ca^{2+} uptake.

143BΔcytb cells had a ~ 50% lower NAD^+/NADH ratio than 143Bwt cells (fig. S4A), as previously reported (*16*). Exposure to XeB increased the NAD^+/NADH ratio by twofold at 1 hour in both cell lines, which further increased by fivefold in 143BΔcytb cells at 4 hours (Fig. 3H). By comparison, the mitochondrial uncoupler carbonyl cyanide *p*-trifluoromethoxyphenylhydrazone (FCCP) (1 μM, 1 hour) caused a twofold increase in both cell lines (Fig. 3H). Similar results were observed in RCC4 cells (fig. S2G). To determine whether the observed NAD^+/NADH ratio change in response to XeB was localized to mitochondria, we used two-photon microscopy to determine the fluorescence intensity ratio between flavin adenine dinucleotide (FAD) and pyridine nucleotides [NAD(P)H]. This optical redox ratio correlates with the oxidation-reduction state (*42*, *43*) and NAD^+/NADH ratio (*44*). A 4-hour XeB treatment significantly increased the optical redox ratio (Fig. 3, I and J), confirming that NAD^+/NADH changed in mitochondria where αKGDH is located. To determine whether there was also a change in cytoplasmic NAD^+/NADH, we transfected cells with the NAD^+/NADH sensor peredox (*45*). XeB significantly increased the NAD^+/NADH ratio, presented here as the difference between the red-to-green fluorescence signal at the beginning and end of the experiment (fig. S4, B and C). Together, these data confirm that the NAD^+/NADH ratio increases in both the mitochondria and cytoplasm when Ca^{2+} transfer from the ER to mitochondria is inhibited.

The greater XeB-induced increase in the NAD^+/NADH ratio observed in the 143BΔcytb compared with 143Bwt cells is consistent with higher basal NADH production through the activity of αKGDH required for reductive carboxylation in the143BΔcytb cells. The XeB-induced increase in the NAD^+/NADH ratio is of similar magnitude to that caused by siRNA-mediated knockdown of αKGDH (*20*). These results further suggest that αKGDH activity depends on mitochondrial matrix Ca^{2+} supplied by low-level $InsP_3R$-mediated Ca^{2+} release. To test this, we reasoned that XeB-induced reduction of αKGDH activity and associated cell death could be reversed by supplying sufficient substrates to elevate flux through αKGDH by mass action. We first supplied methyl-pyruvate because it can be converted to acetyl-CoA and citrate, which can be used for reductive metabolism to generate metabolic intermediates needed for growth of the OXPHOS-deficient 143BΔcytb cells. Furthermore, high concentrations of methyl-pyruvate will generate a substrate mass-action effect to accelerate the activity of αKGDH independently of allosteric regulation by Ca^{2+}. Addition of methyl-pyruvate to the growth medium prevented XeB-induced cell death in both cell lines. Dimethyl-α-ketoglutarate rescues other OXPHOS-defective cells that rely on glutamine-derived anapleurosis in a manner dependent on αKGDH activity (*17*). Similarly, addition of dimethyl-α-ketoglutarate to enhance αKGDH activity by mass action also markedly reduced XeB-induced death in the 143BΔcytb cells (Fig. 3K). To determine whether constitutive ER-to-mitochondrial Ca^{2+} transfer was generally required by other OXPHOS-deficient cells that rely on reductive carboxylation, we induced reductive carboxylation in 143Bwt and Hela cells by impairing OXPHOS by treatment with antimycin A (*16*).

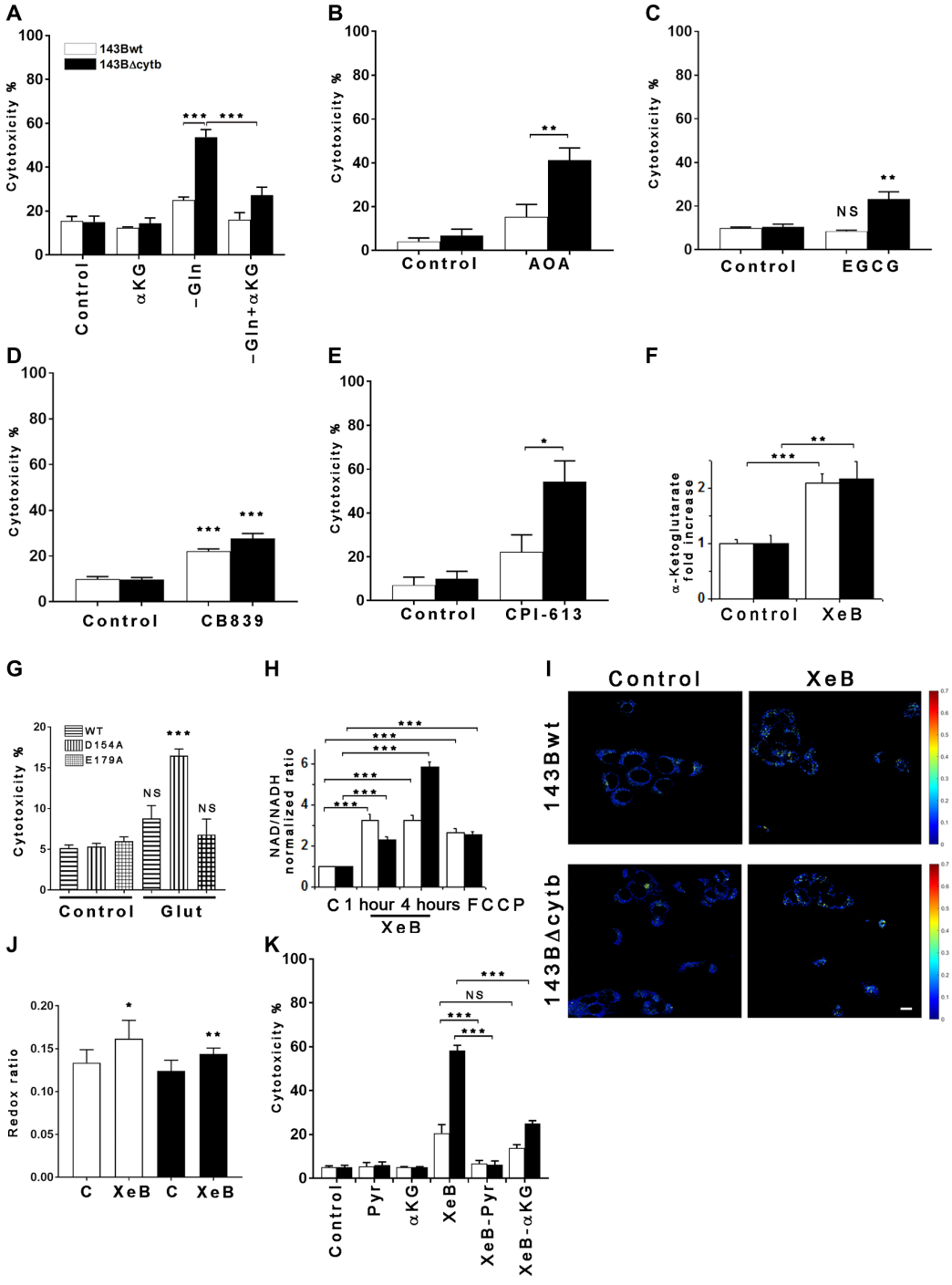

Fig. 3. Inhibition of constitutive $InsP_3R$-mediated Ca^{2+} release reduces αKGDH activity, enhances the NAD^+/NADH ratio, and increases cell death that can be rescued by metabolic intermediates. (**A**) Cells were cultured in normal media (control), glutamine-free media (−Gln), or glutamine-free media supplemented with 5 mM dimethyl-α-ketoglutarate (−Gln+αKG), and cell death was determined by propidium iodide incorporation. Means ± SEM of three independent experiments, each in triplicate. ***$P < 0.001$ compared to respective control. (**B**) Cells were treated with 1 mM aminotransferase inhibitor aminooxyacetate (AOA), and cell death was determined by propidium iodide incorporation. Means ± SEM of three independent experiments, each in triplicate. **$P < 0.01$ compared to respective control. (**C**) Cells were treated with 50 μM glutamate dehydrogenase (GDH) inhibitor epigallocatechin gallate (EGCG), and cell death was determined by propidium iodide incorporation. Means ± SEM of three independent experiments, each in triplicate. **$P < 0.01$ compared to respective control. (**D**) Cells were treated with 5 μM glutaminase inhibitor CB839, and cell death was determined by propidium iodide incorporation. Means ± SEM of three independent experiments, each in triplicate. **$P < 0.01$ compared to respective control. (**E**) Cells were treated with 0.5 mM αKGDH inhibitor CPI-613, and cell death was determined by propidium iodide incorporation. Means ± SEM of three independent experiments, each in triplicate. *$P < 0.05$ compared to respective control. (**F**) Cells were treated with 5 μM XeB (4 hours), and αKG levels were determined. Means ± SEM of three independent experiments each performed in triplicate. **$P < 0.01$ and ***$P < 0.001$ compared to respective control. (**G**) 143B cells transfected with a WT E1 subunit of the αKGDH or the D154A or E179A mutants were cultured with glutamine as the only carbon source for 24 hours, and cell death was determined by propidium iodide incorporation. Means ± SEM of three independent experiments, each in triplicate. ***$P < 0.001$ compared to respective control. (**H**) Cells were treated with 5 μM XeB for 1 and 4 hours or with 1 μM FCCP for 1 hour, and the NAD^+/NADH ratio was determined. Means ± SEM of three independent experiments each performed in triplicate. ***$P < 0.001$ compared to respective control. (**I**) Representative maps of redox ratio in 143Bwt and 143BΔcytb treated or not with 5 μM XeB for 4 hours. (**J**) Bar graph represents quantification of the redox ratio. Means ± SD of three independent experiments. *$P < 0.05$ and **$P < 0.01$ compared to respective control. (**K**) Cell death assessed by LDH release in cells treated with 5 μM XeB for 12 hours in the presence of 5 mM dimethyl-α-ketoglutarate (αKG) or 5 mM methyl-pyruvate (Pyr). Means ± SEM of three independent experiments each performed in triplicate. ***$P < 0.001$ compared to respective control.

Antimycin A reduced OCR and elevated ECAR (fig. S4, D to G) similar to the 143BΔcytb and RCC4 cells, and the treated cells became more sensitive to XeB-induced cytotoxicity (fig. S4, H and I). Antimycin A–treated Hela cells also exhibited enhanced cytotoxicity in response to AOA and CPI-613, similar to 143BΔcytb cells (fig. S4, J and K). Together, these data suggest that αKGDH maintains metabolic homeostasis in OXPHOS-defective cancer cells by enabling the use of glutamine for reductive carboxylation and that this activity depends on constitutive ER-to-mitochondria Ca^{2+} transfer.

Table 1. Inhibition of constitutive $InsP_3R$-mediated Ca^{2+} release decreases reductive carboxylation metabolites downstream of αKGDH. Untargeted metabolomics was performed on OXPHOS-defective 143BΔcytb cells treated or not with 5 μM XeB for 4 hours, and the fold change of relevant reductive carboxylation metabolites related to αKGDH were analyzed. Means ± SEM of three independent experiments each with three replicates.

Metabolite	Fold change	*P* value
Malic acid	0.70 ± 0.032	0.0479*
Succinate	0.66 ± 0.037	0.0034**
αKG	0.80 ± 0.15	0.2693
Citrate-isocitrate	0.86 ± 0.07	0.0442*
Aconitase	1.08 ± 0.026	0.1025

Inhibition of $InsP_3R$-mediated Ca^{2+} release in OXPHOS-defective cells activates SIRT1-mediated prosurvival autophagy

Inhibition of $InsP_3R$ activity and Ca^{2+} uptake by mitochondria induces prosurvival autophagy in several cell lines (*23*, *24*). Inhibition of $InsP_3R$ activity with XeB or by simultaneous RNA interference knockdown of types 1 and 3 $InsP_3R$ (Fig. 4, A and B) or knockdown of MCU (Fig. 4C) induced autophagy in both 143Bwt and 143BΔcytb cells. Similar results were observed in RCC4 + *vhl* and RCC4 cells (fig. S2H). Autophagy plays a prosurvival role in both cell lines because exposure to XeB in the presence of the autophagy inhibitors 3-methyladenine (3MA) (Fig. 4D) or chloroquine (CQ; fig. S5A) caused profound cell death (Fig. 4E).

In normal cells and cancer cells with functional mitochondria, inhibition of Ca^{2+} transfer to mitochondria reduces ATP levels and activates AMPK in addition to activating autophagy (*23*, *24*). Unexpectedly, inhibition and/or knockdown of $InsP_3R$ or MCU activated AMPK in both 143Bwt and 143BΔcytb cells (fig. S5, B to D). This activation was associated with an increased AMP/ATP ratio in the 143Bwt cells (fig. S5, E to G), whereas the AMP/ATP ratio was unchanged in the 143BΔcytb cells (fig. S5, E to G), as expected, because ATP levels in these cells are independent of OXPHOS. Thus, mechanisms other than a fall in ATP must be responsible for enhanced AMPK activity observed in the 143BΔcytb cells. Because NAD^+ levels are increased by inhibition of Ca^{2+} transfer to mitochondria (Fig. 3, H to J) and autophagy can be regulated by the NAD^+-dependent deacetylase SIRT1 (*31*), we examined the possible involvement of SIRT1 in XeB-induced autophagy. Global acetylation levels were depressed by XeB, as shown by a reduction in the acetylation of a 53-kDa protein (Fig. 4F), a molecular weight that corresponds to p53, a known SIRT1 substrate (*46*), which was confirmed by Western blot (fig. S5, H and I). The SIRT1 inhibitor EX527 suppressed the reduction in p53 acetylation caused by XeB (Fig. 4F and fig. S5, H and I). EX527 reduced XeB-induced autophagy in both 143Bwt and 143BΔcytb cell lines, as shown by Western blot (Fig. 4, G and H) and immunofluorescence (Fig. 4I) without altering AMPK phosphorylation (fig. S5, J and K). The levels of SIRT1 were similar in both 143Bwt and 143BΔcytb cell lines (fig. S6A), and SIRT1 was located in both the cytoplasm and nucleus to a similar extent (fig. S6B). To confirm a role of SIRT1 in XeB-induced autophagy, we treated mouse embryonic fibroblasts (MEFs) lacking SIRT1 (*SIRT1*$^{-/-}$ cells) (fig. S6C) with XeB and monitored the formation of autophagosomes with mCherry–green fluorescent protein (GFP)–LC3. *SIRT1*$^{-/-}$ cells were unable to mount an autophagic response, as evidenced by the absence of autophagosomal-puncta formation (fig. S6, D and E). In contrast, autophagosome formation was significantly enhanced in SIRT1-expressing wild-type MEFs, confirming that SIRT1 was necessary for XeB-induced autophagy. Inhibition of SIRT1 activity by EX527 increased cell death in both 143Bwt and 143BΔcytb cell lines (Fig. 4J), as well as in RCC4 cells (fig. S2I). These results suggest that elevated NAD^+ levels activate SIRT1 to induce prosurvival autophagy in response to inhibition of ER-to-mitochondrial Ca^{2+} transfer.

Whereas inhibition of constitutive Ca^{2+} transfer from ER to mitochondria activated prosurvival autophagy in both 143wt and 143BΔcytb cells, 143BΔcytb cells were protected to a lesser extent (Fig. 4, A to E). To understand the basis for the enhanced cytotoxicity observed in the 143BΔcytb cells, we measured autophagic flux in both cell lines. Both lines were treated with CQ, which inhibits fusion of autophagosomes with lysosomes (*47*). Under these conditions, autophagosomal components, including LC3-II, cannot be degraded and accumulate. CQ caused LC3-II to accumulate to similar extents in both cell lines (Fig. 5A). XeB caused a strong and additive increase in LC3-II accumulation in CQ-treated 143Bwt cells (Fig. 5A), indicating enhanced autophagic flux. In contrast, the CQ- and XeB-induced increases were not additive in 143BΔcytb cells (Fig. 5A), suggesting that autophagic flux was compromised. To confirm this interpretation, we used tandem-tagged mCherry-GFP-LC3. When autophagosomes containing mCherry-GFP-LC3 fuse to lysosomes, GFP fluorescence is quenched, whereas the red fluorescence from mCherry remains. Observation of a mix of yellow and red puncta is indicative of enhanced autophagic flux (*48*), whereas defective lysosomal fusion results in the accumulation of yellow puncta. Inhibition of $InsP_3R$-mediated Ca^{2+} release by XeB induced the appearance of a mix of yellow and red puncta in 143Bwt cells (Fig. 5, B and C). In contrast, 143BΔcytb cells accumulated only yellow puncta (Fig. 5, B and C). This result suggests that inhibition of constitutive Ca^{2+} release enhances autophagic flux in cells with normal OXPHOS, as previously reported, whereas there is a defect in autophagosome-lysosome fusion in 143BΔcytb cells. To determine whether defective autophagosome-lysosome fusion was specific to 143BΔcytb cells or was a consequence of their metabolic reliance on reductive carboxylation, reductive carboxylation was induced in Hela cells by treatment with antimycin A. As in the 143BΔcytb cells, XeB-induced autophagy in the antimycin A–treated Hela cells caused an accumulation of yellow autophagosomal puncta (fig. S6, F and G). We speculated that because autophagy provides necessary metabolites to maintain cellular homeostasis (*49*), impaired autophagic flux in cells with defective OXPHOS in response to decreased Ca^{2+} transfer to mitochondria likely increases metabolic stress that results in the observed enhanced cytotoxicity in these cells. Cells with defective OXPHOS are deficient in aspartate synthesis necessary for nucleoside synthesis (*18*, *19*). Addition of nucleosides as a metabolic substrate to the media prevented XeB-induced cell death in both cell lines (Fig. 5D).

DISCUSSION

Whereas the role of mitochondrial Ca^{2+} in regulating OXPHOS is well established, its role in regulating other mitochondrial metabolic pathways is less clearly understood. Here, we explored the role of

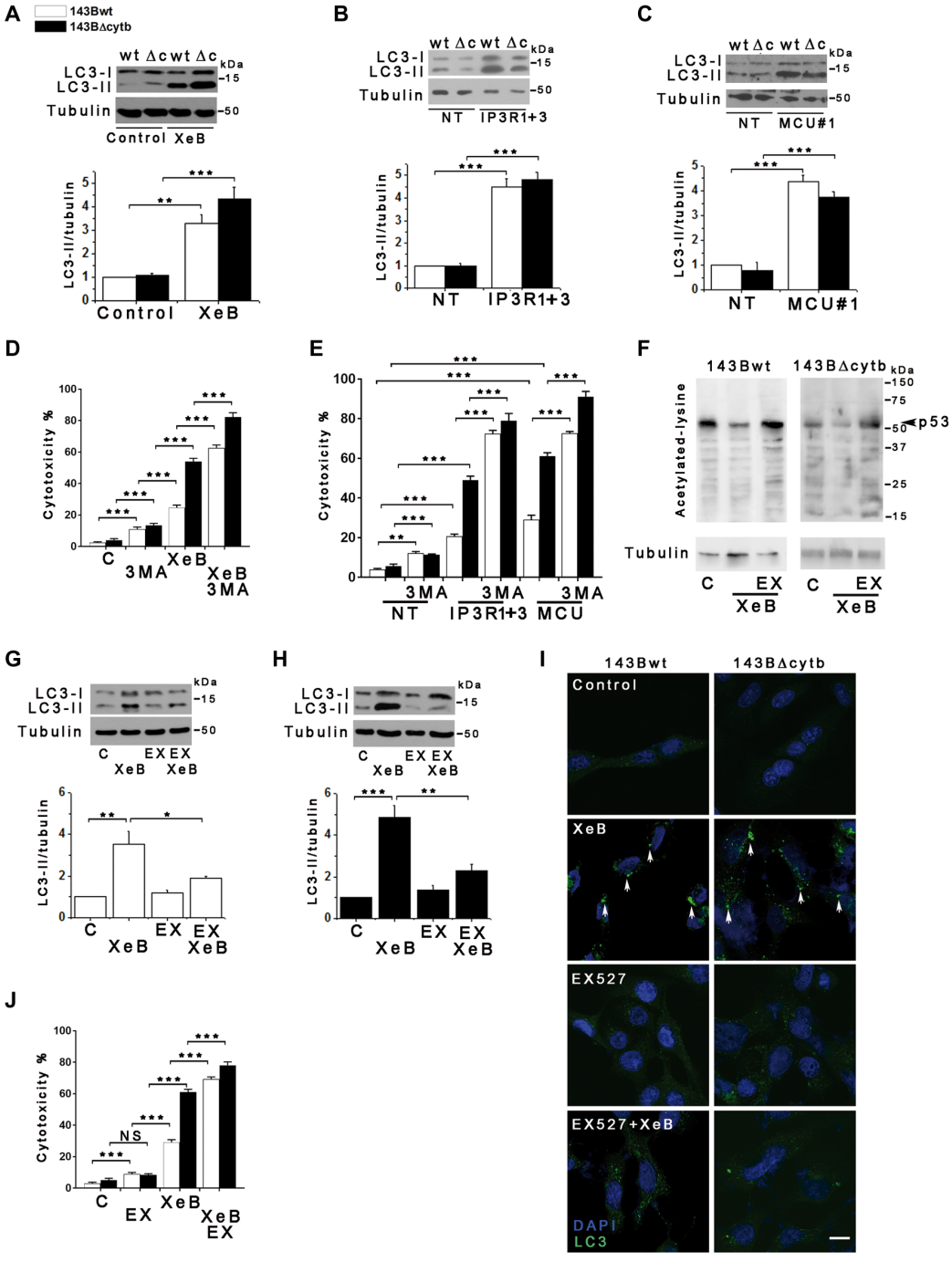

Fig. 4. Inhibition of constitutive $InsP_3R$-mediated Ca^{2+} release increases SIRT1-dependent deacetylation and autophagy. (**A**) Representative Western blots of the autophagy marker LC3 or tubulin as loading control in 143Bwt (wt) and 143BΔcytb (Δc) cell lines treated with 5 μM XeB for 4 hours. (**B**) As in (A) but with cells transfected with siRNA against types 1 and 3 $InsP_3R$ (IP3R1 + 3) or a nontargeting siRNA for 24 hours. (**C**) As in (A) but with cells transfected with a siRNA against MCU or a nontargeting siRNA for 72 hours. Bar graphs in (A), (B), and (C) represent quantification of LC3-II/tubulin expressed as means ± SEM of three independent experiments. (**D**) Cell death as assessed by LDH release in cells treated with 5 μM XeB and/or 3-methyladenine (3MA) or vehicle control (C) for 12 hours. (**E**) As in (D) but with cells transiently transfected with a siRNA against MCU, types 1 and 3 $InsP_3R$ (IP3R1 + 3) or a nontargeting siRNA and treated or not with 3MA for 12 hours. Cytotoxicity data in (D) and (E) are means ± SEM of three independent experiments, each with six replicates. (**F**) Representative Western blots of four independent experiments to determine pan-acetylated lysine or tubulin in cells under basal conditions (C) or pretreated with 10 μM of the SIRT1 inhibitor EX527 (EX) for 12 hours and then exposed to 5 μM XeB for 4 hours. (**G**) Representative Western blots of LC3 and tubulin in 143Bwt cells under basal conditions (C) exposed or not to 10 μM EX527 (EX) for 12 hours and then treated with 5 μM XeB for 4 hours. (**H**) As in (G) in 143BΔcytb cells. Bar graphs in (G) and (H) represent quantification of LC3-II/tubulin expressed as means ± SEM of three independent experiments. (**I**) Representative immunofluorescence images of three independent experiments showing LC3 puncta formation (arrows) in cells under basal conditions (control) or pretreated with 10 μM EX527 for 12 hours and then exposed to 5 μM XeB for 4 hours. Scale bar, 10 μm. (**J**) Cell death as assessed by LDH release in cells under basal conditions (C) or exposed to 10 μM EX527 (EX) for 12 hours and then treated with 5 μM XeB for 4 hours. Results represent means ± SEM of three independent experiments. For all experiments, $^*P < 0.05$, $^{**}P < 0.01$, and $^{***}P < 0.001$ compared to respective control.

ER-to-mitochondrial Ca^{2+} transfer on metabolism and viability of cells with defective capacity for OXPHOS. We found that despite impaired OXPHOS, mitochondrial matrix Ca^{2+} remained a critical regulator of mitochondrial metabolism and viability because of the Ca^{2+} sensitivity of αKGDH activity. In addition, we found that the bioenergetic crisis induced by interruption of mitochondrial Ca^{2+} uptake was sensed by SIRT1, which played a prosurvival role by triggering NAD^+-dependent autophagy that was not fully functional in cells with defective OXPHOS. Our results suggest that mitochondrial matrix Ca^{2+} plays a fundamental role in cellular bioenergetics by regulating both OXPHOS-dependent and OXPHOS-independent metabolic pathways. The discovery of a role for Ca^{2+} in regulating OXPHOS-independent pathways may have consequences for cancer cell metabolism and possible therapeutic implications.

Matrix Ca^{2+} concentration regulates mitochondrial bioenergetics, in part, by modulating the activities of the respiratory chain, PDH and two TCA cycle dehydrogenases, NAD^+-IDH, and αKGDH. In cells with functional mitochondria, constitutive ER-to-mitochondrial

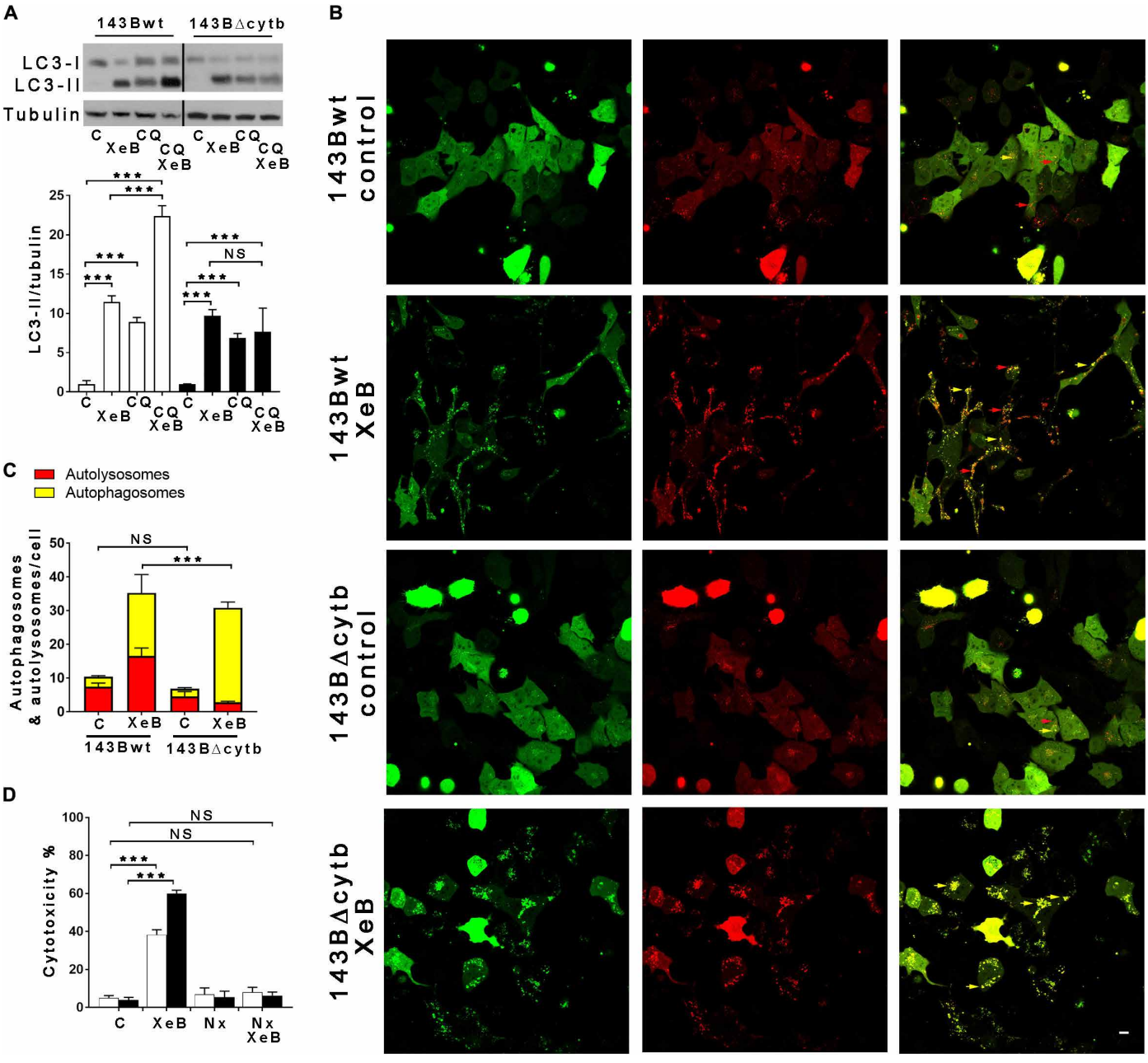

Fig. 5. Autophagy flux is impaired in OXPHOS-defective cells. (**A**) Representative Western blots of autophagy marker LC3 and tubulin as loading control in 143Bwt (wt) and 143BΔcytb (Δc) cell lines treated with 5 μM XeB for 4 hours in the presence of the autophagy inhibitor chloroquine (CQ). Bar graphs represent quantification of LC3-II/tubulin expressed as means ± SEM of three independent experiments. ***$P < 0.001$ compared to respective control. (**B**) Representative images of 143Bwt (wt) and 143BΔcytb (Δc) cell lines transfected with mCherry-GFP-LC3 for 24 hours, followed by exposure to 5 μM XeB for 4 hours. Arrows indicate autophagosome (yellow) and autolysosome (red). Scale bar, 10 μm. (**C**) Number of autolysosomes (red) and autophagosome (yellow) per cell. Results represent means ± SEM of three independent experiments. At least 100 cells per experiment were counted. ***$P < 0.001$ compared to respective control. (**D**) Cell death by LDH release in cells under basal conditions (C) or exposed to 5 μM XeB for 4 hours in the presence of nucleosides (Nx). Means ± SEM of three independent experiments. ***$P < 0.001$ compared to respective control.

transfer of Ca^{2+} supports the activity of PDH as a key enzyme that controls carbon flux into the TCA cycle. In the absence of this transfer, Ca^{2+}-activated PDH phosphatase activity decreases, resulting in PDH hyperphosphorylation and diminished activity, limiting flux of pyruvate into the TCA cycle. αKGDH oxidizes αKG to succinyl-CoA, CO_2, and NADH, providing reducing equivalents for OXPHOS (*50*). Diminished TCA cycle production of NADH leads to lower rates of OXPHOS, and ATP levels decline (*23*). Tumorigenic breast, prostate, and melanoma cancer cells behave similarly (*24*), supporting the concept that many cancer cells also rely on mitochondrial metabolism for ATP generation (*1*, *2*, *51*, *52*). Whether matrix Ca^{2+} plays an important role in mitochondrial bioenergetics beyond its role in regulating OXPHOS has been unknown. To explore the role of matrix Ca^{2+} in regulating mitochondrial pathways

in addition to OXPHOS, we examined 143BΔcytb cells as a model for cells that have defective OXPHOS. αKGDH plays a central role in these cells as a gatekeeper for utilization of glutamine-derived carbon for oxidation and reductive carboxylation, with its importance in cancer cell metabolism well recognized (*6*, *7*, *20*, *40*, *51*). Many cancers display oncogene-dependent addiction to glutamine that has been exploited therapeutically (*53*). Through glutaminase activity, glutamine provides glutamate that is converted by glutamate dehydrogenases or aminotransferases to αKG (*2*). When oxidation of metabolites in the TCA cycle is unfavorable, such as in the presence of defective OXPHOS activity or hypoxia, many cancer cells use glutamine-derived αKG through reductive carboxylation to generate citrate for lipid synthesis and four-carbon intermediates needed to produce other TCA cycle metabolites (*40*). The oxidation of αKG through αKGDH in these circumstances remains essential because it is necessary to generate the reducing equivalents necessary to maintain reductive carboxylation (*20*). Of the Ca^{2+}-sensitive enzymes in the TCA cycle, only αKGDH contributes to generation of metabolites in cells performing reductive carboxylation, including 143BΔcytb cells (*16*). αKGDH inhibition impairs the viability of several cancer cell lines (*54*, *55*) and breast cancer–associated lung metastasis (*56*).

We found that inhibition of $InsP_3R$-mediated Ca^{2+} release or mitochondrial Ca^{2+} uptake decreased αKGDH activity in both OXPHOS-competent 143Bwt cells and OXPHOS-defective 143BΔcytb cells, as evidenced by αKG accumulation and an increased NAD^+/NADH ratio. Similar accumulation of αKG suggests that αKGDH activity is comparable in both cell lines, in accordance with the similar glutamine consumption rates in these cells (*16*). Accumulation of αKG in response to reduced mitochondrial Ca^{2+} uptake in 143Bwt cells is consistent with the Ca^{2+} dependence of αKGDH activity. Reductive carboxylation of αKG is mediated by NADP-IDH2, which is not Ca^{2+} sensitive (*57*). Thus, αKG accumulation observed in 143BΔcytb cells is likely caused by restricted availability of reducing equivalents, which are normally generated by Ca^{2+}-dependent αKGDH oxidation of αKG and are necessary to fuel IDH2-mediated reductive carboxylation of αKG. Inhibition of $InsP_3R$ activity induced a larger increase in the NAD^+/NADH ratio in 143BΔcytb cells compared with 143Bwt cells, consistent with a higher rate of NADH consumption in 143BΔcytb cells to sustain their higher rates of reductive carboxylation (*20*).

As shown previously, inhibition of $InsP_3R$ Ca^{2+} signaling and mitochondrial Ca^{2+} uptake induces a bioenergetic crisis that results in activation of prosurvival autophagy. Similar responses were observed for the OXPHOS-competent and OXPHOS-incompetent cells used here. Previously, we demonstrated that activation of AMPK, due to an elevated adenosine diphosphate/ATP ratio, is upstream of autophagy activation (*23*). Here, we found that inhibition of constitutive ER-to-mitochondria Ca^{2+} transfer was associated with an elevated NAD^+/NADH ratio that was sensed by SIRT1. Pharmacological and genetic inhibition of SIRT1 repressed autophagy, indicating that SIRT1 was also upstream of autophagy activation. Prolonged inhibition of mitochondrial Ca^{2+} uptake reduced the viability of both 143Bwt and 143BΔcytb cells. Cell death was prevented by incubation with cell-permeable methyl-pyruvate, dimethyl-αKG, and nucleosides, suggesting that it was caused by deficits in mitochondrial bioenergetics. The relatively minor cytotoxicity observed in 143Bwt cells was likely due to an effective AMPK-dependent (*23*) and SIRT1-dependent prosurvival autophagic response to inhibition of OXPHOS caused by reduced activities of PDH and TCA cycle dehydrogenases (*24*). The enhanced death rate of 143BΔcytb cells may be accounted for by two, not mutually exclusive mechanisms. First, the combination of OXPHOS inhibition (reduced ATP and Ψ_m) and lack of essential TCA cycle–derived metabolic intermediates derived from reductive carboxylation, due to the central role of Ca^{2+}-dependent αKGDH activity in this process, may critically compromise cell viability. We considered that the higher sensitivity of 143BΔcytb cells could be the result of excessive ROS production, but we observed no differences between the two cell lines, in agreement with other reports (*6*, *38*), and the antioxidant NAC did not confer protection. In contrast, the two cell lines differed in their autophagic responses to their distinct metabolic challenges. Whereas increased autophagic flux in 143Bwt cells culminated in the delivery of autophagosomal cargo to lysosomes, autophagic flux in the 143BΔcytb cells was aborted, leaving autophagosome accumulation in the cytoplasm as a consequence of a failure to fuse with lysosomes. Because autophagy as a survival mechanism requires lysosomal-mediated hydrolysis reactions to recycle metabolic intermediates for use elsewhere in the cell, diminished autophagosome-lysosome fusion is expected to limit the availability of lysosome-derived metabolites necessary for cell death protection. The lack of both lysosome-derived metabolic intermediates and TCA-derived metabolites together may create conditions that are highly cytotoxic in OXPHOS-defective cells. The mechanisms that limit autophagosome-lysosome fusion specifically in 143BΔcytb cells remain to be determined. Alterations in mitochondrial function caused by chemical inhibition of the electron transport chain impairs lysosomal activity and induces accumulation of large vacuoles (*58*), but this seems unlikely to account for our observations because those effects are mediated by ROS, which were produced at similar levels in 143Bwt and 143BΔcytb cells. $CD4^+$ T lymphocytes with defective mitochondrial function caused by genetic deletion of the mitochondrial transcription factor Tfam show dysfunctional lysosomes and impaired endolysosomal trafficking and autophagy. However, in contrast to our results, those phenotypes are associated with a reduced NAD^+/NADH ratio, and restoration of NAD^+ levels improves lysosomal function (*59*). However, these results do suggest that cell redox state may fine-tune lysosomal function and play a role in 143BΔcytb cells.

In summary, the results in the present study show that inhibition of constitutive mitochondrial Ca^{2+} uptake elevates NAD^+ by reducing αKGDH activity, which promotes SIRT1 activation that, in turn, activates autophagy as a prosurvival mechanism. In cells with defective OXPHOS, impaired autophagosome-lysosome fusion exacerbates metabolic stress, rendering these cells more sensitive to cell death. Our results highlight a central role of αKGDH and OXPHOS in cancer cells and suggest that the mechanisms involved in ER-to-mitochondria Ca^{2+} transfer offer new therapeutic targets for cancer.

MATERIALS AND METHODS

Reagents

The LC3B (#2775), acetylated-lysine (#9441), acetyl-p53 (#2525), phospho-AMPK (#2535), AMPK (#5831), SIRT1 (#2493), and p53 (#2527) antibodies were from Cell Signaling Technology. The β-tubulin (#556321) and $InsP_3R$-3 (#610313) antibodies were from BD Biosciences. The MCU (#HPA016480) and c-Myc (#M4439) antibodies were from Sigma-Aldrich. The $InsP_3R$-1 (ABS55) antibody was from Millipore. Anti-OGDH (2-oxoglutarate dehydrogenase) rabbit polyclonal (#GTX33374) was from GeneTex. Nuclei were stained with

Hoechst. Peroxidase-conjugated secondary antibodies were purchased from Amersham (#NA934 and #NA931). 3MA, methyl-pyruvate, dimethyl-α-ketoglutarate, antimycin A, FCCP, oligomycin, rotenone, 2DG, and Hank's balanced salt solution (HBSS) were from Sigma-Aldrich. CPI-613 and EX527 were from Tocris Biosciences. Fluo-4 AM, NAO, and Hoechst were from Thermo Fisher Scientific. EGCG and CB839 were from Selleckchem. XeB was extracted and purified from the marine sponge *Xestospongia exigua* as described (*32*).

Cell culture and transfection

Osteosarcoma 143Bwt and 143BΔcytb cybrid cells, provided by N. S. Chandel (Northwestern University), were cultured in Dulbecco's modified Eagle's medium (DMEM) supplemented with 10% fetal bovine serum (FBS), uridine (100 μg/ml), 1 mM pyruvate, penicillin (100 U ml^{-1}), streptomycin (100 μg ml^{-1}), and fungizone (0.25 μg ml^{-1}; Gibco) at 37°C (95%/5% air/CO_2). Hela cells were grown in similar conditions in the absence of uridine and pyruvate. Wild-type and *SIRT1*$^{-/-}$ cells, provided by Leonard Guarente (Massachusetts Institute of Technology), were cultured in similar conditions as 143B cells. Pharmacological inhibition of OXPHOS in 143Bwt and Hela cells was achieved by adding 1 μM antimycin A (complex III inhibitor) to the culture media for 48 hours, as described (*16*). Transfections of siRNA were performed with a Nucleofector electroporator (Amaxa Biosystems). siRNAs against MCU and types 1 and 3 $InsP_3Rs$ were previously described (*23*) and purchased from GE Healthcare Dharmacon. To simultaneously silence type 1 and type 3 $InsP_3R$, a specific siRNA was designed (GE Healthcare Dharmacon), which consisted of 5′-GUGAGAAGCAGAAGAAGGAUU-3′ and 3′-UUCACUCUUCGUCUUCUUCCU-5′. pAAV-CAG-Peredox was a gift from G. Yellen (Addgene plasmid # 73807; http://n2t.net/addgene:73807; RRID:Addgene_73807).

Ca^{2+} signals

Imaging of spontaneous changes in cytoplasmic Ca^{2+} concentration ($[Ca^{2+}]_c$) was accomplished by total internal reflection fluorescence (TIRF) microscopy using a Nikon eclipse Ti inverted TIRF microscope equipped with an apo TIRF 60×, 1.49 numerical aperture (NA) lens with a stage-top Tokai Hit incubator. Cells were loaded with freshly prepared Fluo-4 (5 μM) and imaged at 37°C and 5% CO_2 ~100 nm into the cell. The gain on the Andor iXon EMCCD camera was set to maximum, and images were collected every 50 ms for 2 min. For simultaneous measurements of $[Ca^{2+}]_c$ and mitochondrial matrix $[Ca^{2+}]$ ($[Ca^{2+}]_m$), 143B cells were grown on 25-mm glass coverslips for 48 hours and then loaded with 2 μM rhod-2/AM (50 min) and 5 μM Fluo-4/AM (30 min) in extracellular medium as described (*25*). Coverslips were mounted in an open chamber and imaged. After 25 s of baseline recording, an $InsP_3$ mobilizing agonist (histamine, 100 μM) was added and confocal images were recorded every 3 s (510 Meta; Carl Zeiss) at 488- and 561-nm excitation using a ×63 oil objective. Images were analyzed and quantified using ImageJ (National Institutes of Health).

Site-directed mutagenesis

Mutagenesis of recombinant human OGDH cDNA in the Myc-DDK–tagged vector was performed using the QuikChange site-directed mutagenesis kit (Stratagene, La Jolla, CA) as per the manufacturer's instructions and as previously described (*60*). For the OGDHD154A-myc mutant, the primers were 5′-CCC TGG GGA TTT TGG CTG CTG ATC TGG ACT C-3′ and 5′-GAC TCC AGA TCA GCA GCC AAA ATC CCC AGG G-3′. For OGDHE179A-myc, the primers were 5′-TTC TAT GGC CTG GAT GCG TCT GAC CTC GAC AAG-3′ and 5′-CTT GTC GAG GTC AGA CGC ATC CAG GCC ATA GAA-3′. All mutants were checked by DNA sequencing, and their expression was analyzed by immunoblot and immunofluorescence assays.

Western blotting and treatments

Drugs were added in fresh media as indicated. Treatments were terminated by rapid removal of medium with cells on ice, followed by cell lysis with CytoBuster protein extraction reagent (Novagen) supplemented with protease and phosphatase inhibitors (cOmplete PhosSTOP, Roche). Protein extracts were separated in 4, 10, or 15% SDS-polyacrylamide gels and transferred to polyvinylidene difluoride membranes (Millipore). Blocking was performed at room temperature for 1 hour in 5% fat-free milk, and membranes were incubated overnight at 4°C with primary antibody and then for 1 hour at room temperature with a secondary antibody conjugated to horseradish peroxidase. Chemiluminescence detection used ECL Plus reagent (Pierce) and a series of timed exposure images were acquired with a FluorChem Q system (ProteinSimple) to ensure that densitometric analyses were performed at exposures within the linear range. To ensure equal protein loading across gels, membranes were submerged in stripping buffer (Restore Western Blot Stripping Buffer; Pierce), incubated at 37°C for 20 min, and reprobed with a loading control antibody. ImageJ was used for densitometric analysis.

Cellular oxygen consumption and ECARs

OCR and ECAR as measurements of OXPHOS and glycolysis, respectively, were measured at 37°C using an XF^{e}96 extracellular analyzer (Agilent, USA). A total of 1.5×10^4 cells per well were seeded onto poly-lysine (Sigma-Aldrich, USA) pretreated plates and allowed to attach for 24 hours. Where indicated, 143Bwt and 143BΔcytb cells were exposed either to 5 μM XeB or vehicle for 4 hours and then loaded into the analyzer in fresh unbuffered Seahorse media, and basal OCR and ECAR were determined. Sequential injections of 1 μM oligomycin, 50 nM FCCP, and 1 μM rotenone/antimycin A were used to reveal different parameters of cellular respiration.

Immunofluorescence

Cells were fixed in 100% methanol at −20°C for 12 min, blocked in 1% bovine serum albumin, and incubated overnight with LC3B antibody (Cell Signaling technology, #2775). Alexa Fluor 488 secondary antibody (Molecular Probes, #A-11008) was incubated for 1 hour at room temperature, and cells were mounted in ProLong Gold antifade with DAPI (4′,6-diamidino-2-phenylindole; Molecular Probes, #P36931). Visual examination was performed on a Zeiss Axiovert 510 LSM Pascal confocal microscope using a high–numerical aperture water immersion 63× objective.

Optical redox ratio calculation

Microscopy images were collected using a Leica TCS SP8 confocal microscope system equipped with an Insight DS+ Ti:Sapphire laser (Spectra-Physics) for multiphoton near-infrared (NIR) excitation. Two-photon excitation fluorescence images were obtained at excitation wavelengths of 755 and 860 nm, with average powers of 18 and 29 mW at the sample, respectively. Two emission channels were recorded simultaneously on a pair of nondescanned Leica HyD hybrid

detectors, using a fluorescein isothiocyanate/DAPI fluorescence filter cube equipped with a 680-nm short-pass entrance filter and emission band-pass filters at 460 ± 25 nm (NADH channel) and 525 ± 25 nm (FAD channel). A Leica DMi8 inverted microscope was used with a Leica HC PL IRAPO 40×/1.10 water immersion objective optimized for confocal NIR microscopy. Images were collected with a 1.5× zoom magnification factor and sampled using 8-bit dynamic range and 1024 × 1024 pixels (corresponding to a 194 μm by 194 μm field of view, or 0.189 μm/pixel). Bidirectional raster scans were conducted at a line rate of 600 Hz and averaging each line eight times per image. For each of the four types of samples studied (ΔcytB and wt cells, both XeB treated and untreated), images were collected from three wells in a multiwell glass-bottomed dish, and sampling between three to five different regions of interest within each well. Fluorescence intensity images of NAD(P)H and FAD were normalized on the basis of the illumination power and averaging. The background and weak nucleus fluorescence were removed using a binary mask with Otsu's threshold method to exclude noise from signal not pertaining to metabolism. After co-registering the fluorescence intensity images using cross-correlation, the pixel-wise optical ratio [FAD/(FAD + NAD(P)H] was calculated and the mean value per field was compared (*61*).

Peredox

Peredox-mCherry was transfected into cells using FuGene according to the manufacturer's protocol and imaged in live cells 12 hours later. Peredox is composed of a permuted GFP T-Sapphire (green) interposed between two Rex subunits, with a C-terminal mCherry to normalize for green fluorescence (*45*). Ratiometric imaging (green/red) was performed on a Nikon A1R confocal microscope equipped with Perfect Focus using a 63× plan apo lens/1.4 NA. Peredox increases GFP fluorescence (excitation, 405; emission 520) upon binding to NADH. The green-to-red fluorescence ratio increase, which correlates with an increase in the NADH:NAD^+ ratio, was analyzed using SML software and ImageJ.

Mitochondrial membrane potential

Cells were loaded with tetramethylrhodamine methyl ester (TMRM; Life Technologies; 5 nM) for 30 min at 37°C and 5% CO_2. Hoechst 33342 was used as a nuclear counterstain. Images were acquired using a Nikon C2+ spectral confocal microscope using the same settings for all experiments. TMRM fluorescence was quantified with ImageJ software.

Determination of ROS levels

The generation of intracellular oxidative stress was determined using the dihydroethidium (DHE) probe as previously described (*62*). 143Bwt and 143BΔcytb cells were grown in complete media, seeded in 12-well plates, and allowed to attach overnight. The next day, the cells were exposed for 4 hours to ethanol (control) or 5 μM XeB, and then, the culture medium was replaced by a solution containing 5 μM DHE in HBSS and incubated for 20 min in the dark. After this, the cells were washed, trypsinized, and resuspended in 500 μl of HBSS and measured by FACS Calibur flow cytometer.

Determination of NAD^+/NADH ratio and αKG levels

All measurements were performed using commercial kits (BioVision, K337-100; K677-100) according to the manufacturer's instructions. Briefly, cells were incubated either with 5 μM XeB or vehicle for 1 or 4 hours, washed twice with phosphate-buffered saline (PBS), scraped off the dishes, and pelleted. For NAD^+/NADH ratio, NAD^+ and NADH were extracted and the samples were subjected to two freeze-thaw cycles and centrifuged. Aliquots of each sample were heated at 60°C for 30 min to decompose NAD^+. Samples were then loaded into 96-well plates for absorbance measurements at 450 nm. To determine αKG levels, samples were deproteinized with 7% perchloric acid, neutralized with a buffer solution (3 M KOH, 0.4 M tris, and 3 M KCl), and converted to pyruvate. Background pyruvate was subtracted. The reaction was incubated at 37°C for 30 min, and optical density was measured at 570 nm.

Metabolomics

Subconfluent culture dishes were incubated for 4 hours in DMEM containing 15 mM glucose, 2 mM glutamine, and 10% FBS in the presence or absence of 5 μM XeB. Cells were then washed twice with ice-cold saline and overlaid with 500 μl of cold methanol/water (50/50, v/v), transferred to an Eppendorf tube and subjected to three freeze-thaw cycles. After rigorous vortexing, the debris was pelleted by centrifugation at 16,000*g* and 4°C for 15 min. Pellets were used for protein quantitation (BCA Protein Assay; Thermo Fisher Scientific). The supernatant was transferred to a new tube and evaporated to dryness using a SpeedVac concentrator (Thermo Savant, Holbrook, NY). Metabolites were reconstituted in 100 μl of 0.03% formic acid in analytical-grade water, vortex-mixed, and centrifuged to remove debris. Thereafter, the supernatant was transferred to a high-performance liquid chromatography (HPLC) vial for the metabolomics study. Targeted metabolite profiling was performed using a liquid chromatography–mass spectrometry/mass spectrometry (LC-MS/MS) approach as described before (*20*). Briefly, metabolites were reconstituted in 100 μl of 0.03% formic acid in LC-MS–grade water, vortex-mixed, and centrifuged to remove debris. LC-MS/MS and data acquisition were performed using an AB QTRAP 5500 LC/triple quadrupole mass spectrometer (Applied Biosystems SCIEX) with an injection volume of 20 μl. Chromatogram review and peak area integration were performed using MultiQuant software version 2.1 (Applied Biosystems SCIEX). The peak area for each detected metabolite was normalized against the total ion count of each sample and the mean for each metabolite within the sample batch of each run to correct for variations introduced by sample handling through instrument analysis. The normalized areas were used as variables for the multivariate analyses and modeling using SIMCA-P (version 13.0.1; Umetrics). The processed datasets were mean-centered, unit-variance–scaled, and then applied to principal components analysis to evaluate the clustering and to detect outliers. Univariate statistical differences of the metabolites between two groups were analyzed using Student's *t* test. The pathway enrichment analysis of differential metabolites between two groups was performed using Metaboanalyst 3.0 (http://metaboanalyst.ca).

Determination of intracellular ATP levels

ATP levels were determined with CellTiter-Glo Luminescent Cell Viability Assay kit (Promega, USA). 143Bwt and 143BΔcytb cells (1×10^5 cells/ml) were seeded into 96-well plates and incubated for 4 hours in culture medium in the absence (vehicle, ethanol) or presence of 5 μM XeB, 1 μM antimycin A, and 1 μM oligomycin. After exposure, cells were washed twice with PBS to remove the medium and resuspended in 20 μl of PBS. Bioluminescence was measured on a BioTek luminometer.

AMP/ATP ratio

Nucleotides were extracted using perchloric acid, neutralized, and frozen for subsequent HPLC analysis. AMP and ATP were quantified using ion pair reverse-phase HPLC, with a C18 RP column, under isocratic elution conditions in 200 mM phosphate, 5 mM tetrabutylammonium phosphate, and 3% acetonitrile.

Cell death assays

Lactate dehydrogenase (LDH) released from dying cells was determined by a colorimetric assay (Roche). Propidium iodide incorporation (5 mg/ml) was determined by flow cytometry (BD FACSAria III).

Statistics

All statistical analyses were performed using GraphPad Prism 4.03 (GraphPad Software, San Diego, CA, USA). The data are expressed as means ± SEM of three independent experiments, each one performed in technical triplicate. Statistical analysis was performed using unpaired *t* tests, one-way analysis of variance (ANOVA) with Bonferroni's post-test for pairwise comparisons, or two-way ANOVA. The data were considered statistically significant at the 95% level ($P < 0.05$).

SUPPLEMENTARY MATERIALS

stke.sciencemag.org/cgi/content/full/13/640/eaay1212/DC1

Fig. S1. Mitochondrial parameters and simultaneous knockdown of types 1 and 3 $InsP_3R$ induces cell death in OXPHOS-defective 143BΔcytb cells.

Fig. S2. Pseudohypoxic RCC4 cells rely on constitutive $InsP_3R$-mediated Ca^{2+} signals.

Fig. S3. Inhibition of constitutive $InsP_3R$-mediated Ca^{2+} transfer to the mitochondria substantially changes the metabolomic profile of 143BΔcytb cell lines.

Fig. S4. OXPHOS-defective cells rely on constitutive $InsP_3R$-mediated Ca^{2+} signals.

Fig. S5. Inhibition of constitutive $InsP_3R$-mediated Ca^{2+} release reduces αKGDH activity and activates SIRT1 and AMPK.

Fig. S6. SIRT1 is necessary for the autophagy induced by inhibition of Ca^{2+} transfer to mitochondria.

View/request a protocol for this paper from *Bio-protocol*.

REFERENCES AND NOTES

1. W. H. Koppenol, P. L. Bounds, C. V. Dang, Otto Warburg's contributions to current concepts of cancer metabolism. *Nat. Rev. Cancer* **11**, 325–337 (2011).
2. N. N. Pavlova, C. B. Thompson, The emerging hallmarks of cancer metabolism. *Cell Metab.* **23**, 27–47 (2016).
3. K. E. Wellen, C. B. Thompson, A two-way street: Reciprocal regulation of metabolism and signalling. *Nat. Rev. Mol. Cell Biol.* **13**, 270–276 (2012).
4. A. Carracedo, L. C. Cantley, P. P. Pandolfi, Cancer metabolism: Fatty acid oxidation in the limelight. *Nat. Rev. Cancer* **13**, 227–232 (2013).
5. S. M. Sanderson, J. W. Locasale, Revisiting the Warburg effect: Some tumors hold their breath. *Cell Metab.* **28**, 669–670 (2018).
6. F. Weinberg, R. Hamanaka, W. W. Wheaton, S. Weinberg, J. Joseph, M. Lopez, B. Kalyanaraman, G. M. Mutlu, G. R. S. Budinger, N. S. Chandel, Mitochondrial metabolism and ROS generation are essential for Kras-mediated tumorigenicity. *Proc. Natl. Acad. Sci. U.S.A.* **107**, 8788–8793 (2010).
7. C. S. Ahn, C. M. Metallo, Mitochondria as biosynthetic factories for cancer proliferation. *Cancer Metab.* **3**, 1 (2015).
8. C. Jose, N. Bellance, R. Rossignol, Choosing between glycolysis and oxidative phosphorylation: A tumor's dilemma? *Biochim. Biophys. Acta* **1807**, 552–561 (2011).
9. R. Moreno-Sanchez, A. Marín-Hernández, E. Saavedra, J. P. Pardo, S. J. Ralph, S. Rodríguez-Enríquez, Who controls the ATP supply in cancer cells? Biochemistry lessons to understand cancer energy metabolism. *Int. J. Biochem. Cell Biol.* **50**, 10–23 (2014).
10. M. V. Liberti, J. W. Locasale, The Warburg effect: How does it benefit cancer cells? *Trends Biochem. Sci.* **41**, 211–218 (2016).
11. M. G. Vander Heiden, R. J. DeBerardinis, Understanding the intersections between metabolism and cancer biology. *Cell* **168**, 657–669 (2017).
12. L. Ippolito, A. Morandi, M. L. Taddei, M. Parri, G. Comito, A. Iscaro, M. R. Raspollini, F. Magherini, E. Rapizzi, J. Masquelier, G. G. Muccioli, P. Sonveaux, P. Chiarugi, E. Giannoni, Cancer-associated fibroblasts promote prostate cancer malignancy via metabolic rewiring and mitochondrial transfer. *Oncogene* **38**, 5339–5355 (2019).
13. A. Naguib, G. Mathew, C. R. Reczek, K. Watrud, A. Ambrico, T. Herzka, I. C. Salas, M. F. Lee, N. El-Amine, W. Zheng, M. E. Di Francesco, J. R. Marszalek, D. J. Pappin, N. S. Chandel, L. C. Trotman, Mitochondrial complex I inhibitors expose a vulnerability for selective killing of Pten-null cells. *Cell Rep.* **23**, 58–67 (2018).
14. J. R. Molina, Y. Sun, M. Protopopova, S. Gera, M. Bandi, C. Bristow, T. McAfoos, P. Morlacchi, J. Ackroyd, A.-N. A. Agip, G. Al-Atrash, J. Asara, J. Bardenhagen, C. C. Carrillo, C. Carroll, E. Chang, S. Ciurea, J. B. Cross, B. Czako, A. Deem, N. Daver, J. F. de Groot, J.-W. Dong, N. Feng, G. Gao, J. Gay, M. G. Do, J. Greer, V. Giuliani, J. Han, L. Han, V. K. Henry, J. Hirst, S. Huang, Y. Jiang, Z. Kang, T. Khor, S. Konoplev, Y.-H. Lin, G. Liu, A. Lodi, T. Lofton, H. Ma, M. Mahendra, P. Matre, R. Mullinax, M. Peoples, A. Petrocchi, J. Rodriguez-Canale, R. Serreli, T. Shi, M. Smith, Y. Tabe, J. Theroff, S. Tiziani, Q. Xu, Q. Zhang, F. Muller, R. A. DePinho, C. Toniatti, G. F. Draetta, T. P. Heffernan, M. Konopleva, P. Jones, M. E. Di Francesco, J. R. Marszalek, An inhibitor of oxidative phosphorylation exploits cancer vulnerability. *Nat. Med.* **24**, 1036–1046 (2018).
15. W. W. Wheaton, S. E. Weinberg, R. B. Hamanaka, S. Soberanes, L. B. Sullivan, E. Anso, A. Glasauer, E. Dufour, G. M. Mutlu, G. S. Budigner, N. S. Chandel, Metformin inhibits mitochondrial complex I of cancer cells to reduce tumorigenesis. *eLife* **3**, e02242 (2014).
16. A. R. Mullen, W. W. Wheaton, E. S. Jin, P.-H. Chen, L. B. Sullivan, T. Cheng, Y. Yang, W. M. Linehan, N. S. Chandel, R. J. DeBerardinis, Reductive carboxylation supports growth in tumour cells with defective mitochondria. *Nature* **481**, 385–388 (2012).
17. Q. Chen, K. Kirk, Y. I. Shurubor, D. Zhao, A. J. Arreguin, I. Shahi, F. Valsecchi, G. Primiano, E. L. Calder, V. Carelli, T. T. Denton, M. F. Beal, S. S. Gross, G. Manfredi, M. D'Aurelio, Rewiring of glutamine metabolism is a bioenergetic adaptation of human cells with mitochondrial DNA mutations. *Cell Metab.* **27**, 1007–1025.e5 (2018).
18. K. Birsoy, T. Wang, W. W. Chen, E. Freinkman, M. Abu-Remaileh, D. M. Sabatini, An essential role of the mitochondrial electron transport chain in cell proliferation is to enable aspartate synthesis. *Cell* **162**, 540–551 (2015).
19. L. B. Sullivan, D. Y. Gui, A. M. Hosios, L. N. Bush, E. Freinkman, M. G. Vander Heiden, Supporting aspartate biosynthesis is an essential function of respiration in proliferating cells. *Cell* **162**, 552–563 (2015).
20. A. R. Mullen, Z. Hu, X. Shi, L. Jiang, L. K. Boroughs, Z. Kovacs, R. Boriack, D. Rakheja, L. B. Sullivan, W. M. Linehan, N. S. Chandel, R. J. DeBerardinis, Oxidation of alpha-ketoglutarate is required for reductive carboxylation in cancer cells with mitochondrial defects. *Cell Rep.* **7**, 1679–1690 (2014).
21. S. Strumilo, Short-term regulation of the alpha-ketoglutarate dehydrogenase complex by energy-linked and some other effectors. *Biochemistry* **70**, 726–729 (2005).
22. J. G. McCormack, R. M. Denton, The effects of calcium ions and adenine nucleotides on the activity of pig heart 2-oxoglutarate dehydrogenase complex. *Biochem. J.* **180**, 533–544 (1979).
23. C. Cárdenas, R. A. Miller, I. Smith, T. Bui, J. Molgó, M. Müller, H. Vais, K.-H. Cheung, J. Yang, I. Parker, C. B. Thompson, M. J. Birnbaum, K. R. Hallows, J. K. Foskett, Essential regulation of cell bioenergetics by constitutive $InsP_3$ receptor Ca^{2+} transfer to mitochondria. *Cell* **142**, 270–283 (2010).
24. C. Cárdenas, M. Müller, A. McNeal, A. Lovy, F. Jaña, G. Bustos, F. Urra, N. Smith, J. Molgó, J. A. Diehl, T. W. Ridky, J. K. Foskett, Selective vulnerability of cancer cells by inhibition of Ca^{2+} transfer from endoplasmic reticulum to mitochondria. *Cell Rep.* **14**, 2313–2324 (2016).
25. K. Mallilankaraman, C. Cárdenas, P. J. Doonan, H. C. Chandramoorthy, K. M. Irrinki, T. Golenár, G. Csordás, P. Madireddi, J. Yang, M. Müller, R. Miller, J. E. Kolesar, J. Molgó, B. Kaufman, G. Hajnóczky, J. K. Foskett, M. Madesh, MCUR1 is an essential component of mitochondrial Ca^{2+} uptake that regulates cellular metabolism. *Nat. Cell Biol.* **14**, 1336–1343 (2012).
26. K. Mallilankaraman, P. Doonan, C. Cárdenas, H. C. Chandramoorthy, M. Müller, R. Miller, N. E. Hoffman, R. K. Gandhirajan, J. Molgó, M. J. Birnbaum, B. S. Rothberg, D.-O. D. Mak, J. K. Foskett, M. Madesh, MICU1 is an essential gatekeeper for MCU-mediated mitochondrial Ca^{2+} uptake that regulates cell survival. *Cell* **151**, 630–644 (2012).
27. J. K. Foskett, B. Philipson, The mitochondrial Ca^{2+} uniporter complex. *J. Mol. Cell. Cardiol.* **78**, 3–8 (2015).
28. I. Marin-Valencia, C. Yang, T. Mashimo, S. Cho, H. Baek, X.-L. Yang, K. N. Rajagopalan, M. Maddie, V. Vemireddy, Z. Zhao, L. Cai, L. Good, B. P. Tu, K. J. Hatanpaa, B. E. Mickey, J. M. Matés, J. M. Pascual, E. A. Maher, C. R. Malloy, R. J. DeBerardinis, R. M. Bachoo, Analysis of tumor metabolism reveals mitochondrial glucose oxidation in genetically diverse human glioblastomas in the mouse brain in vivo. *Cell Metab.* **15**, 827–837 (2012).
29. Y.-R. Kim, J.-I. Baek, S. H. Kim, M.-A. Kim, B. Lee, N. Ryu, K.-H. Kim, D.-G. Choi, H.-M. Kim, M. P. Murphy, G. Macpherson, Y.-S. Choo, J. Bok, K.-Y. Lee, J.-W. Park, U.-K. Kim, Therapeutic potential of the mitochondria-targeted antioxidant MitoQ in mitochondrial-ROS induced sensorineural hearing loss caused by Idh2 deficiency. *Redox Biol.* **20**, 544–555 (2019).
30. S. Rodríguez-Enríquez, S. C. Pacheco-Velázquez, Á. Marín-Hernández, J. C. Gallardo-Pérez, D. X. Robledo-Cadena, I. Hernández-Reséndiz, J. D. García-García, J. Belmont-Díaz, R. López-Marure, L. Hernández-Esquivel, R. Sánchez-Thomas, R. Moreno-Sánchez, Resveratrol inhibits cancer cell proliferation by impairing oxidative phosphorylation and inducing oxidative stress. *Toxicol. Appl. Pharmacol.* **370**, 65–77 (2019).

31. R. Moreno-Sánchez, S. Rodríguez-Enríquez, A. Marín-Hernández, E. Saavedra, Energy metabolism in tumor cells. *FEBS J.* **274**, 1393–1418 (2007).
32. C. Cárdenas, J. L. Liberona, J. Molgó, C. Colasante, G. A. Mignery, E. Jaimovich, Nuclear inositol 1,4,5-trisphosphate receptors regulate local Ca^{2+} transients and modulate cAMP response element binding protein phosphorylation. *J. Cell Sci.* **118**, 3131–3140 (2005).
33. J. Q. Kwong, M. S. Henning, A. A. Starkov, G. Manfredi, The mitochondrial respiratory chain is a modulator of apoptosis. *J. Cell Biol.* **179**, 1163–1177 (2007).
34. C. Pierro, S. J. Cook, T. C. F. Foets, M. D. Bootman, H. L. Roderick, Oncogenic K-Ras suppresses IP_3-dependent Ca^{2+} release through remodelling of the isoform composition of IP_3Rs and ER luminal Ca^{2+} levels in colorectal cancer cell lines. *J. Cell Sci.* **127**, 1607–1619 (2014).
35. K. Shibao, M. J. Fiedler, J. Nagata, N. Minagawa, K. Hirata, Y. Nakayama, Y. Iwakiri, M. H. Nathanson, K. Yamaguchi, The type III inositol 1,4,5-trisphosphate receptor is associated with aggressiveness of colorectal carcinoma. *Cell Calcium* **48**, 315–323 (2010).
36. M. Rana, I. de Coo, F. Diaz, H. Smeets, C. T. Moraes, An out-of-frame cytochrome B gene deletion from a patient with parkinsonism is associated with impaired complex III assembly and an increase in free radical production. *Ann. Neurol.* **48**, 774–781 (2000).
37. S. W. Ryter, H. P. Kim, A. Hoetzel, J. W. Park, K. Nakahira, X. Wang, A. M. K. Choi, Mechanisms of cell death in oxidative stress. *Antioxid. Redox Signal.* **9**, 49–89 (2007).
38. E. L. Bell, N. S. Chandel, Genetics of mitochondrial electron transport chain in regulating oxygen sensing. *Methods Enzymol.* **435**, 447–461 (2007).
39. D. R. Wise, P. S. Ward, J. E. S. Shay, J. R. Cross, J. J. Gruber, U. M. Sachdeva, J. M. Platt, R. G. DeMatteo, M. C. Simon, C. B. Thompson, Hypoxia promotes isocitrate dehydrogenase-dependent carboxylation of α-ketoglutarate to citrate to support cell growth and viability. *Proc. Natl. Acad. Sci. U.S.A.* **108**, 19611–19616 (2011).
40. C. M. Metallo, P. A. Gameiro, E. L. Bell, K. R. Mattaini, J. Yang, K. Hiller, C. M. Jewell, Z. R. Johnson, D. J. Irvine, L. Guarente, J. K. Kelleher, M. G. Vander Heiden, O. Iliopoulos, G. Stephanopoulos, Reductive glutamine metabolism by IDH1 mediates lipogenesis under hypoxia. *Nature* **481**, 380–384 (2012).
41. C. T. Armstrong, J. L. Anderson, R. M. Denton, Studies on the regulation of the human E1 subunit of the 2-oxoglutarate dehydrogenase complex, including the identification of a novel calcium-binding site. *Biochem. J.* **459**, 369–381 (2014).
42. B. Chance, B. Schoener, R. Oshino, F. Itshak, Y. Nakase, Oxidation-reduction ratio studies of mitochondria in freeze-trapped samples. NADH and flavoprotein fluorescence signals. *J. Biol. Chem.* **254**, 4764–4771 (1979).
43. B. Chance, B. Thorell, Localization and kinetics of reduced pyridine nucleotide in living cells by microfluorometry. *J. Biol. Chem.* **234**, 3044–3050 (1959).
44. Z. Liu, D. Pouli, C. A. Alonzo, A. Varone, S. Karaliota, K. P. Quinn, K. Münger, K. P. Karalis, I. Georgakoudi, Mapping metabolic changes by noninvasive, multiparametric, high-resolution imaging using endogenous contrast. *Sci. Adv.* **4**, eaap9302 (2018).
45. R. Mongeon, V. Venkatachalam, G. Yellen, Cytosolic NADH-NAD^+ redox visualized in brain slices by two-photon fluorescence lifetime biosensor imaging. *Antioxid. Redox Signal.* **25**, 553–563 (2016).
46. J. Yi, J. Luo, SIRT1 and p53, effect on cancer, senescence and beyond. *Biochim. Biophys. Acta* **1804**, 1684–1689 (2010).
47. M. Mauthe, I. Orhon, C. Rocchi, X. Zhou, M. Luhr, K.-J. Hijlkema, R. P. Coppes, N. Engedal, M. Mari, F. Reggiori, Chloroquine inhibits autophagic flux by decreasing autophagosome-lysosome fusion. *Autophagy* **14**, 1435–1455 (2018).
48. N. Mizushima, T. Yoshimori, B. Levine, Methods in mammalian autophagy research. *Cell* **140**, 313–326 (2010).
49. U. Ahumada-Castro, E. Silva-Pavez, A. Lovy, E. Pardo, J. Molgó, C. Cárdenas, MTOR-independent autophagy induced by interrupted endoplasmic reticulum-mitochondrial Ca^{2+} communication: A dead end in cancer cells. *Autophagy* **15**, 358–361 (2018).
50. L. Tretter, V. Adam-Vizi, Alpha-ketoglutarate dehydrogenase: A target and generator of oxidative stress. *Philos. Trans. R. Soc. Lond. B Biol. Sci.* **360**, 2335–2345 (2005).
51. R. J. DeBerardinis, N. Sayed, D. Ditsworth, C. B. Thompson, Brick by brick: Metabolism and tumor cell growth. *Curr. Opin. Genet. Dev.* **18**, 54–61 (2008).
52. S. Jia, X. Xu, S. Zhou, Y. Chen, G. Ding, L. Cao, Fisetin induces autophagy in pancreatic cancer cells via endoplasmic reticulum stress- and mitochondrial stress-dependent pathways. *Cell Death Dis.* **10**, 142 (2019).
53. D. R. Wise, C. B. Thompson, Glutamine addiction: A new therapeutic target in cancer. *Trends Biochem. Sci.* **35**, 427–433 (2010).
54. V. I. Bunik, G. Mkrtchyan, A. Grabarska, H. Oppermann, D. Daloso, W. L. Araujo, M. Juszczak, W. Rzeski, L. Bettendorff, A. R. Fernie, J. Meixensberger, A. Stepulak, F. Gaunitz, Inhibition of mitochondrial 2-oxoglutarate dehydrogenase impairs viability of cancer cells in a cell-specific metabolism-dependent manner. *Oncotarget* **7**, 26400–26421 (2016).
55. S. D. Stuart, A. Schauble, S. Gupta, A. D. Kennedy, B. R. Keppler, P. M. Bingham, Z. Zachar, A strategically designed small molecule attacks alpha-ketoglutarate dehydrogenase in tumor cells through a redox process. *Cancer Metab.* **2**, 4 (2014).
56. S. Atlante, A. Visintin, E. Marini, M. Savoia, C. Dianzani, M. Giorgis, D. Sürün, F. Maione, F. Schnütgen, A. Farsetti, A. M. Zeiher, M. Bertinaria, E. Giraudo, F. Spallotta, C. Cencioni, C. Gaetano, α-Ketoglutarate dehydrogenase inhibition counteracts breast cancer-associated lung metastasis. *Cell Death Dis.* **9**, 756 (2018).
57. R. M. Denton, W. A. Hughes, Pyruvate dehydrogenase and the hormonal regulation of fat synthesis in mammalian tissues. *Int. J. Biochem.* **9**, 545–552 (1978).
58. J. Demers-Lamarche, G. Guillebaud, M. Tlili, K. Todkar, N. Bélanger, M. Grondin, A. P. Nguyen, J. Michel, M. Germain, Loss of mitochondrial function impairs lysosomes. *J. Biol. Chem.* **291**, 10263–10276 (2016).
59. F. Baixauli, R. Acín-Pérez, C. Villarroya-Beltrí, C. Mazzeo, N. Nuñez-Andrade, E. Gabandé-Rodriguez, M. D. Ledesma, A. Blázquez, M. A. Martin, J. M. Falcón-Pérez, J. M. Redondo, J. A. Enríquez, M. Mittelbrunn, Mitochondrial respiration controls lysosomal function during inflammatory T cell responses. *Cell Metab.* **22**, 485–498 (2015).
60. M. Cáceres, L. Ortiz, T. Recabarren, A. Romero, A. Colombo, E. Leiva-Salcedo, D. Varela, J. Rivas, I. Silva, D. Morales, C. Campusano, O. Almarza, F. Simon, H. Toledo, K.-S. Park, J. S. Trimmer, O. Cerda, TRPM4 Is a novel component of the adhesome required for focal adhesion disassembly, migration and contractility. *PLOS ONE* **10**, e0130540 (2015).
61. C. A. Alonzo, S. Karaliota, D. Pouli, Z. Liu, K. P. Karalis, I. Georgakoudi, Two-photon excited fluorescence of intrinsic fluorophores enables label-free assessment of adipose tissue function. *Sci. Rep.* **6**, 31012 (2016).
62. F. A. Urra, F. Muñoz, M. Córdova-Delgado, M. P. Ramírez, B. Peña-Ahumada, M. Rios, P. Cruz, U. Ahumada-Castro, G. Bustos, E. Silva-Pavez, R. Pulgar, D. Morales, D. Varela, J. P. Millas-Vargas, E. Retamal, O. Ramírez-Rodríguez, H. Pessoa-Mahana, M. Pavani, J. Ferreira, C. Cárdenas, R. Araya-Maturana, FR58P1a; a new uncoupler of OXPHOS that inhibits migration in triple-negative breast cancer cells via Sirt1/AMPK/β1-integrin pathway. *Sci. Rep.* **8**, 13190 (2018).

Acknowledgments: We thank C. Moraes (University of Miami) and I. F. M. de Coo (Maastricht University) for generating cytochrome b mutant cells, N. S. Chandel (Northwestern University) for providing them, and F. Gonzalez for assistance in the statistical analyses of the data. **Funding:** This work was supported by FONDECYT postdoctoral fellowship nos. 3140458 (F.J.) and 3170813 (F.U.), NIH P30NS047243 (A.L.), FONDECYT nos. 1160332 (C.C.) and 11170291 (F.J.), ANID/FONDAP no. 15150012 (C.C.), NIH R37GM56328 (J.K.F.), NIH S10OD021624 (I.G.), and a grant from the Emerson Collective Cancer Research Fund (J.K.F.). **Author contributions:** C.C. and A.L. designed, performed, and analyzed Seahorse experiments, Ca^{2+} and peredox imaging, immunofluorescence, NAD^+/NADH determinations, metabolomics, and cell death assays. F.U. performed Seahorse experiments and ATP determinations. U.A.-C., G.B., and E.S.-P. designed and performed experiments to determine acetylation levels and the role of SIRT1 in autophagy. C.C., A.L., P.C., and P.F. performed immunofluorescence and Western blotting. M.R. and P.M. performed cell death experiments. C.M., M.H., and I.G. performed and analyzed the optical redox ratio calculation. O.C. designed and performed the site-directed mutagenesis. Analysis of the mutants was performed by E.S.-P., P.M., and P.F. P.F. and E.M. performed cell death experiments in the presence of glutaminolysis inhibitors. H.H. performed immunofluorescence. C.C., A.L., and H.H. performed live-cell detection of autophagy. J.M. and A.Z. interpreted results and provided feedback. A.L., C.C., and J.K.F. participated in experimental design and wrote the manuscript. All authors read and approved the final manuscript. **Competing interests:** The authors declare that they have no competing interests. **Data and materials availability:** All data needed to evaluate the conclusions in the paper are present in the paper or the Supplementary Materials.

Submitted 23 May 2019
Accepted 4 June 2020
Published 14 July 2020
10.1126/scisignal.aay1212

Citation: C. Cardenas, A. Lovy, E. Silva-Pavez, F. Urra, C. Mizzoni, U. Ahumada-Castro, G. Bustos, F. Jaña, P. Cruz, P. Farias, E. Mendoza, H. Huerta, P. Murgas, M. Hunter, M. Rios, O. Cerda, I. Georgakoudi, A. Zakarian, J. Molgó, J. K. Foskett, Cancer cells with defective oxidative phosphorylation require endoplasmic reticulum–to–mitochondria Ca^{2+} transfer for survival. *Sci. Signal.* **13**, eaay1212 (2020).

Science Signaling

Cancer cells with defective oxidative phosphorylation require endoplasmic reticulum–to–mitochondria Ca^{2+} transfer for survival

Cesar Cardenas, Alenka Lovy, Eduardo Silva-Pavez, Felix Urra, Craig Mizzoni, Ulises Ahumada-Castro, Galdo Bustos, Fabian Jana, Pablo Cruz, Paula Farias, Elizabeth Mendoza, Hernan Huerta, Paola Murgas, Martin Hunter, Melany Rios, Oscar Cerda, Irene Georgakoudi, Armen Zakarian, Jordi Molgó and J. Kevin Foskett

Sci. Signal. **13** (640), eaay1212.
DOI: 10.1126/scisignal.aay1212

Staying alive without oxidative phosphorylation

Oxidative phosphorylation is used by many cell types to produce ATP and requires low-level, constitutive Ca^{2+} flow from the ER to the mitochondria. Cardenas *et al.* found that this ER-to-mitochondria Ca^{2+} flow was critical for the survival of cells defective in oxidative phosphorylation, a phenotype that is common in cancer cells. In the absence of oxidative phosphorylation, important metabolites can be generated through reductive carboxylation, a pathway that requires the Ca^{2+}-sensitive enzyme α-ketoglutarate dehydrogenase (αKGDH) and NADH. Manipulations that blocked ER-to-mitochondria Ca^{2+} flow resulted in suppression of αKGDH activity, increases in the NAD^+/NADH ratio, and enhanced autophagy that failed to promote cell survival. These results highlight that mitochondrial Ca^{2+} influx regulates metabolic pathways in addition to oxidative phosphorylation, which could be targeted in specific cancer subtypes.